

# Investigating the Effects of Controllable Parameters on Cold-wire Gas Tungsten Arc Weld Bead Geometry

by

Vladimir Stefanovski

A thesis  
presented to the University of Waterloo  
in fulfillment of the  
thesis requirement for the degree of  
Master of Applied Science  
in  
Mechanical Engineering

Waterloo, Ontario, Canada, 2012

© Vladimir Stefanovski 2012

I hereby declare that I am the sole author of this thesis. This is a true copy of the thesis, including any required final revisions, as accepted by my examiners.

I understand that my thesis may be made electronically available to the public.

## Abstract

Multi-layer Gas Tungsten Arc Welding (GTAW) is widely used for refurbishing plastic injection molds. This welding process can provide the high quality weld that is required for molds that will be subject to high temperatures and pressures during production. This refurbishing weld process is currently performed manually, which exposes the welders to poor working conditions. GTA welding is a tedious and time consuming process when compared to other welding processes. The advantages of automating this process are two-fold: removing workers from arduous working conditions, and decreasing production cycle time by increasing the deposition rate through robotic control. The purpose of this study was to investigate the effects of controllable welding parameters on weld bead geometry for standard welding operating ranges when refurbishing plastic injection molds. Another aim was to determine and predict the sensitivity and response, respectively, of base metal orientation on bead geometry. Remanufactured molds require the removal of tool steel, which can be achieved with current CNC machining technology. However, automating the addition tool steel is difficult achieve due to the inherent complexity of the GTA welding process. The work presented in this thesis is an integral component for simplifying the mold remanufacture process by eliminating the guesswork in choosing optimal welding parameters. Through the means of experimental design and statistical analysis, relationships were developed between welding parameters and their effects on bead height, bead width, penetration, heat affected zone (HAZ) depth and HAZ width. The regression models were capable of predicting responses in bead geometry within 1 millimeter in variation. The resulting regression models can be extended to cold wire GTA welding applications that require high deposition rates and the capabilities of predicting bead geometry for various base metal orientations.

## **Acknowledgements**

My accomplishments are due in large part to the guidance of my supervisor, Dr. Jan Huissoon. I would also like to thank Milica Kovacevic for her patience and support and my colleagues, Ali Sabti, Reza Farshidi and Nikola Stefanovski who have always been around to provide constructive criticism regarding my work. Finally, I would like to thank Tool-Tec Welding Inc. for their cooperation and insight on this topic, and The Ontario Centres of Excellence for their help in funding the project.

## **Dedication**

This thesis is dedicated to my parents Mise and Dina who have always supported and encouraged me throughout my studies.

# Contents

<b>List of Tables</b>	<b>xii</b>
<b>List of Figures</b>	<b>xiv</b>
<b>1 Introduction</b>	<b>1</b>
1.1 GTA welding for Repairing and Refurbishing Injection Molds . . . . .	1
1.1.1 Current Practice . . . . .	1
1.1.2 Manual Gas Tungsten Arc Welding (GTAW) . . . . .	3
1.1.3 Semi-Automated GTA welding . . . . .	6
1.1.4 Fully-Automated GTA welding . . . . .	8
1.2 Literature Review . . . . .	13
<b>2 Measurement Systems</b>	<b>18</b>
2.1 Cross-section Weld Feature Measurement System . . . . .	19
2.1.1 Weld sectioning and sample preparation procedure . . . . .	19
2.1.2 Calibration of Weld Imaging System . . . . .	20

2.1.3	Image Processing for Weld Imaging System . . . . .	22
2.2	Laser Profiler . . . . .	27
2.2.1	Image Processing of Weld Profiler . . . . .	29
2.2.2	Corner Detection Weld bead . . . . .	30
2.2.3	Calibration of Weld Profiler . . . . .	30
2.2.4	Image to World Map . . . . .	32
2.2.5	Accuracy . . . . .	34
<b>3</b>	<b>Pilot Experiment and Analysis</b>	<b>36</b>
3.1	Experimental Design . . . . .	36
<b>4</b>	<b>Main Experiments and Analysis</b>	<b>45</b>
4.1	Parameter levels and experiment design . . . . .	46
4.2	Modeling . . . . .	50
4.3	Analysis of Variance (ANOVA) . . . . .	54
4.4	Results . . . . .	57
4.4.1	Weld Bead Height . . . . .	57
4.4.2	Weld Bead Width . . . . .	58
4.4.3	Weld Bead Penetration . . . . .	59
4.4.4	Weld Heat Affected Zone (HAZ) Depth . . . . .	60
4.4.5	Weld Heat Affected Zone (HAZ) Width . . . . .	61

4.5	Reduced Models . . . . .	62
4.6	Discussion of results . . . . .	71
<b>5</b>	<b>Conclusions and Future Work</b>	<b>80</b>
5.1	Conclusions . . . . .	80
5.2	Future Work . . . . .	81
	<b>Appendix A Experimental Data</b>	<b>83</b>
	<b>Appendix B QQ plots of residuals for Experiment A and B</b>	<b>91</b>
	<b>Appendix C ANOVA Tables</b>	<b>102</b>
	<b>References</b>	<b>114</b>



# List of Tables

3.1	L27 fractional factorial pilot experiment . . . . .	38
3.2	Parameter Levels Pilot Experiment . . . . .	39
3.3	Measurements of L27 Experiment . . . . .	40
3.4	Effects of high and low parameter values on nominal bead geometry . . . . .	41
4.1	Parameter Levels for Experiment A . . . . .	48
4.2	Parameter Levels for Experiment B . . . . .	49
4.3	Analysis of Variance Table . . . . .	54
4.4	Experiment B Results . . . . .	56
4.5	Initial Bead Height ANOVA Table . . . . .	64
4.6	Bead Height ANOVA Table; Removal of $X_1 * X_4$ . . . . .	65
4.7	Bead Height ANOVA Table; Removal of $X_1 * X_5$ . . . . .	65
4.8	Bead Height ANOVA Table; Removal of $X_1 * X_3$ . . . . .	66
4.9	Bead Height ANOVA Table; Removal of $X_2 * X_5$ . . . . .	66
4.10	Bead Height ANOVA Table; Removal of $X_3 * X_4$ . . . . .	67

4.11	Bead Height ANOVA Table; Removal of X3*X4 . . . . .	67
4.12	Comparison of Reduced Models for Bead Height Experiment A . . . . .	67
4.13	Experiment A Model Error . . . . .	73
4.14	Experiment B Model Error . . . . .	74
4.15	Experiment A Reduced Model Results . . . . .	75
4.16	Experiment B Reduced Model Results . . . . .	75
A.1	Measurements of L27 Experiment . . . . .	84
A.2	Measurements of L27 Experiment (cont') . . . . .	85
A.3	GTAW DOE for experiments A and B . . . . .	86
A.4	Experiment A Results . . . . .	87
A.5	Experiment A Results (con't) . . . . .	88
A.6	Experiment B Results . . . . .	89
A.7	Experiment B Results (con't) . . . . .	90
C.1	Analysis of Variance - Bead Height Exp.A . . . . .	102
C.2	Analysis of Variance - Bead Height Exp.B . . . . .	103
C.3	Analysis of Variance - Bead Width Exp.A . . . . .	104
C.4	Analysis of Variance - Bead Width Exp.B . . . . .	104
C.5	Analysis of Variance - Penetration Depth Exp.A . . . . .	105
C.6	Analysis of Variance - Penetration Depth Exp.B . . . . .	105

C.7	Analysis of Variance - HAZ Depth Exp.A . . . . .	106
C.8	Analysis of Variance - HAZ Depth Exp.B . . . . .	106
C.9	Analysis of Variance - HAZ Depth Exp.A . . . . .	107
C.10	Analysis of Variance - HAZ Depth Exp.B . . . . .	108
C.11	Analysis of Variance - HAZ Width Exp.A . . . . .	109
C.12	Analysis of Variance - HAZ Width Exp.B . . . . .	110

# List of Figures

1.1	Manual GTA Welding . . . . .	3
1.2	. . . . .	4
1.3	Equipment for manual GTA welding [1] . . . . .	5
1.4	Schematic diagram of a transverse section of a cold-wire GTA weld bead . . . . .	6
1.5	Simulation of two-dimensional weld layers that make up the final three-dimensional net shape . . . . .	7
1.6	Process flow that is followed for the automated procedure, beginning with computing the CAD difference model, heat and weld path predictions, simulation, validation, and welding. . . . .	8
1.7	An example of a path generation using CNC software substituting cutter diameter by weld pool width for one layer of a three dimensional shape . . . . .	9
1.8	(a) Model of Robot Cell: Power Supply, Robot Controller, ABB IRB4450s, Heating table, Burner controller and PC; (b) Robot gathers joint angles by simulating paths in Robot Studio . . . . .	10

1.9	(a) Milled and polished surface on a volume that was created using 2D software at a thickness of 1 inch; (b) 5ft long, 2D welded surface with 12 layers . . . . .	11
1.10	(a) effects of base metal orientation on bead geometry using fixed weld parameters(b) bead geometry effects compensated using variable weld parameters . . . . .	12
2.1	Original Image of Weld Cross-section . . . . .	21
2.2	Marker on weld specimen . . . . .	21
2.3	Thresholded image of marker . . . . .	22
2.4	(a) Template histogram used for comparison. (b) Composition of histogram	23
2.5	Fuzzy Input Membership Functions . . . . .	24
2.6	Fuzzy Output Membership Functions . . . . .	24
2.7	Histogram Stretching Function . . . . .	24
2.8	Example of Cross-section Segmentation. a) and b) Fuzzy Enhanced Images; c) and ,d) Thresholded images; e,f) Segmented Images . . . . .	26
2.9	MVS Sensor . . . . .	28
2.10	(a) original image of four gauge blocks; (b) pixel intensity distribution of laser stripe; (c) Filtered image, based on location of peak intensity of laser stripe . . . . .	31
2.11	Shortest distance from reference point is edge of weld bead . . . . .	32
2.12	Transformed profile image provides simpler corner detection . . . . .	33

2.13	Calibration data . . . . .	34
3.1	Box plot characteristics stem from normal distribution . . . . .	42
3.2	Box plots for response variables height and width and controllable variables current, voltage, wire feed rate, x orientation and y orientation . . . . .	43
4.1	Welding fixture consisting of all x and y base metal orientations . . . . .	49
4.2	Flow chart for model fitting sequence . . . . .	52
4.3	Main effects of controllable parameters on bead height, where x1, x2, x3, x4, x5 are current, wire feed, robot speed, x-orientation and y-orientation respectivley . . . . .	53
4.4	Measured vs. Predicted Response for Experiment B . . . . .	76
4.5	Average Percentage Error for experiments A and B . . . . .	77
4.6	Boundary ranges containing 95% for models from experiment A and B . . . . .	78

# Chapter 1

## Introduction

The introduction is divided into three sections. First, some background information about the topic is covered followed by a literature review of the application, measurement system and empirical weld models. Finally, an overview of this thesis is stated under research objectives.

### 1.1 GTA welding for Repairing and Refurbishing Injection Molds

#### 1.1.1 Current Practice

The injection molding process is a common method of producing polymer parts at high production rates, with repeatable tolerances, low labor costs and the ability to use a wide range of materials. This process involves feeding polymer material into a heated barrel for mixing, and forcing the molten polymer into a mold where it cools and hardens to

the shape of the mold cavity. Current practice for manufacturing injection molds involves machining a pair of molds called the cavity and core from a large (and expensive) block of tool steel. Mold designers create a CAD model of the mold and then generate tool paths for a CNC milling machine, which removes material from the blocks so that the two mold halves fit together with the required cavity for injection. Usually there are multiple cutter sizes that are used to cut the steel, beginning with a large cutter and progressively decreasing in cutter diameter for more intricate areas. The molds are then benched and polished depending on the desired look of the plastic component. This can range from a shiny glass like surface to a textured imitation leather surface.

When a plastic component is redesigned for a new model product, the mold for the old model can no longer be used to make this component. In the case of small parts, it is often more cost effective to simply scrap the old mold and create a new one based on the new design. However, if the part (and therefore its mold) is large, it is often less expensive to modify the existing mold. A comparison of the CAD model of the original mold with that of the new mold shows where material needs to be added or removed from the original mold to create the new mold. In areas where material needs to be added, the mold surface is first built-up using GTA welding with filler wire, prior to re-machining the mold. The GTA process is preferred because of the high quality and lack of porosity it is capable of producing, which is prerequisite for molds that are exposed to extreme pressures and rapid temperature changes during production. Prior to welding, the mold is heated to 700F (400C) on a preheat table. The heated mold is covered with fiberglass insulation blankets to maintain the high temperature and to protect the welder as depicted in Figure 1.1.

This task is very labour intensive and exposes the welder to high temperatures and poor air quality. Tool-Tec Welding Inc. has been providing this service to the Tool and





Figure 1.1: Manual GTA Welding

Mold industry in the Windsor-Detroit area since 1995, and had been actively pursuing improvements to the process. Following an initial proof-of-concept project sponsored by OCE in 2007, ToolTec was awarded a \$500,000 grant from APMA and a \$250,000 project with the University of Waterloo funded by OCE to develop a fully automated robotic welding cell, a model of which is depicted in Figure 1.2. Unfortunately, ToolTec declared bankruptcy in April 2010, six months before the end of the project, and consequently a number of experiments that had been planned could not be performed.

### **1.1.2 Manual Gas Tungsten Arc Welding (GTAW)**

The arc welding process was developed towards the end of the 19th century and has since been adapted to automated processes through the introduction of robots to industry. A schematic of typical GTA welding equipment is shown in Figure 1.3. Gas Tungsten Arc Welding (GTAW), formerly referred to as Tungsten Inert Gas (TIG) welding, uses a non-consumable tungsten electrode. An electric arc is established between the electrode and workpiece. The weld pool is shielded by an inert shielding gas. The heat from the arc

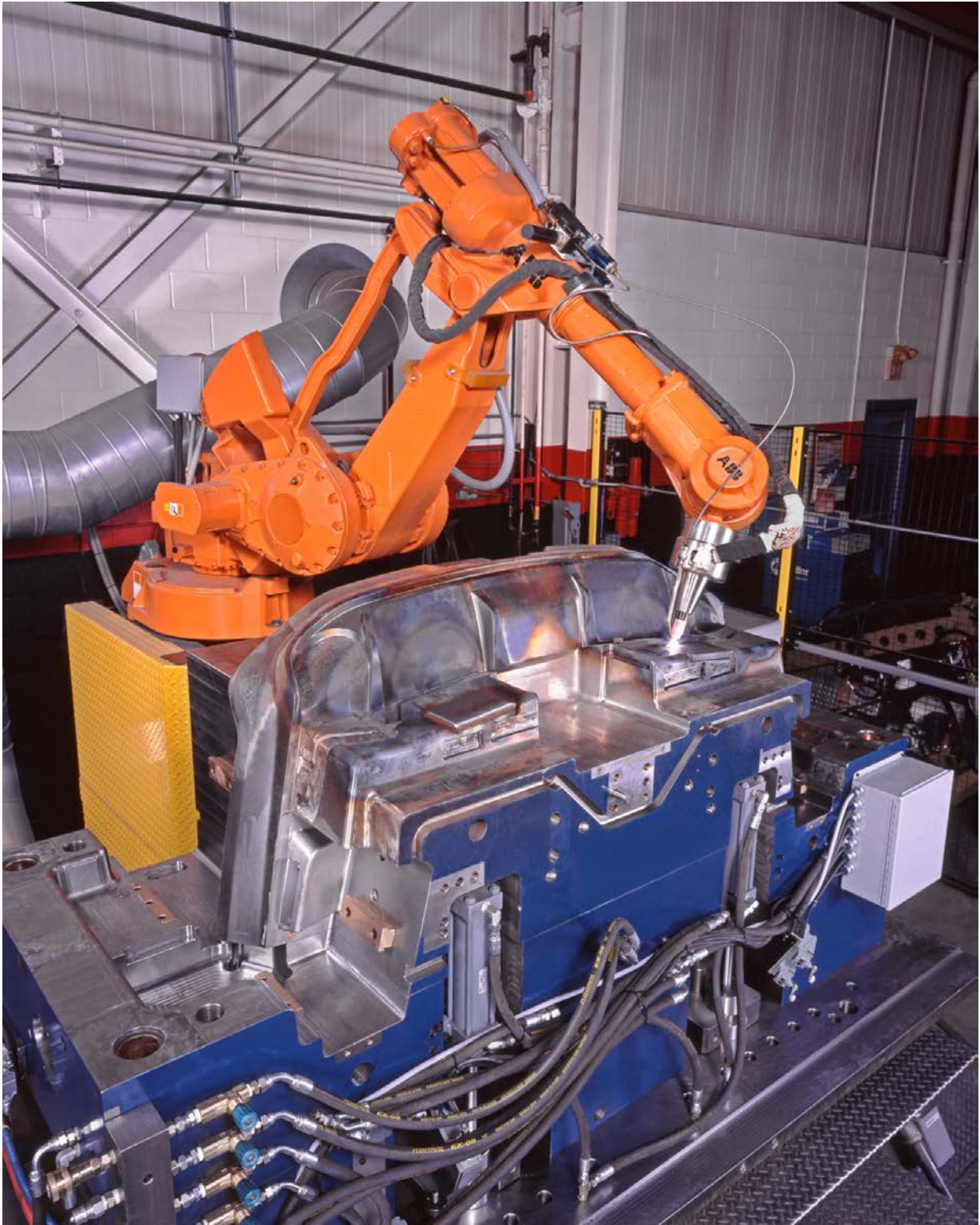


Figure 1.2:  
4

melts the base metal. If additional filler material is required, a separate filler metal wire or rod can be fed into the weld pool either manually or using a wire feeder. This is cold-wire GTAW. Once the welder is satisfied with the size of the weld pool they 'drag' the arc to create a new weld pool (allowing for a 50 percent overlap) and repeat the process.

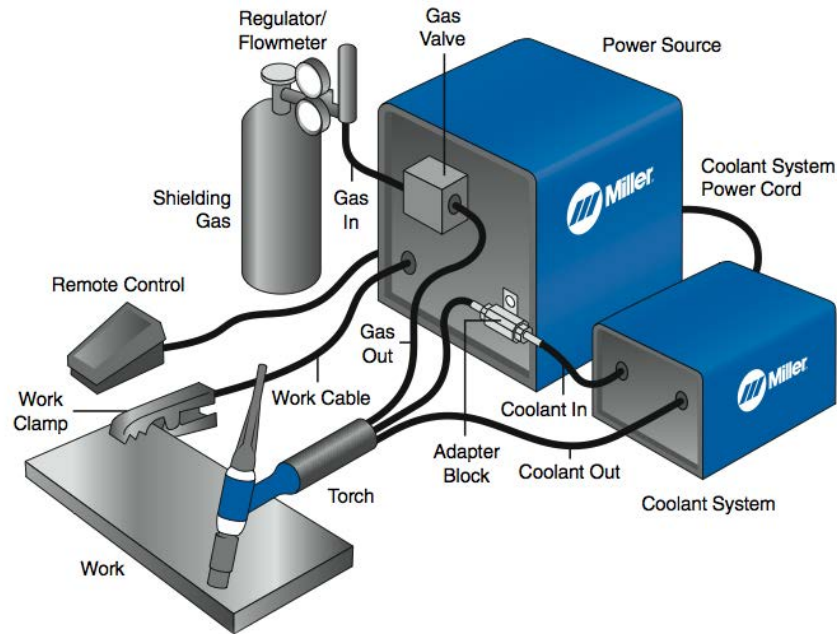


Figure 1.3: Equipment for manual GTA welding [1]

The process parameters involved in GTA welding are categorized into three groups. The first is the group of controllable parameters, which includes welding current, wire feed speed, and travel speed. The second group comprises monitoring variables that are used for feedback during the process such as weld pool geometry, arc gap and temperature. The third group consists of weld bead and penetration geometry, residual stresses and quality, which are the resulting characteristics of the welding process. In manual welding, the first two groups, controllable parameters and sensor variables, are adjusted to achieve

acceptable results in the third group. Figure 1.4 illustrates how the tip of the GTA welding torch, with added filler wire on a base material, is used to create weld bead, pool, and heat affected zone. Automated welding attempts to operate similarly to the manual process, although a good understanding of the controllable parameters and realtime adjustments based on sensor feedback is required to obtain comparable quality and productivity.

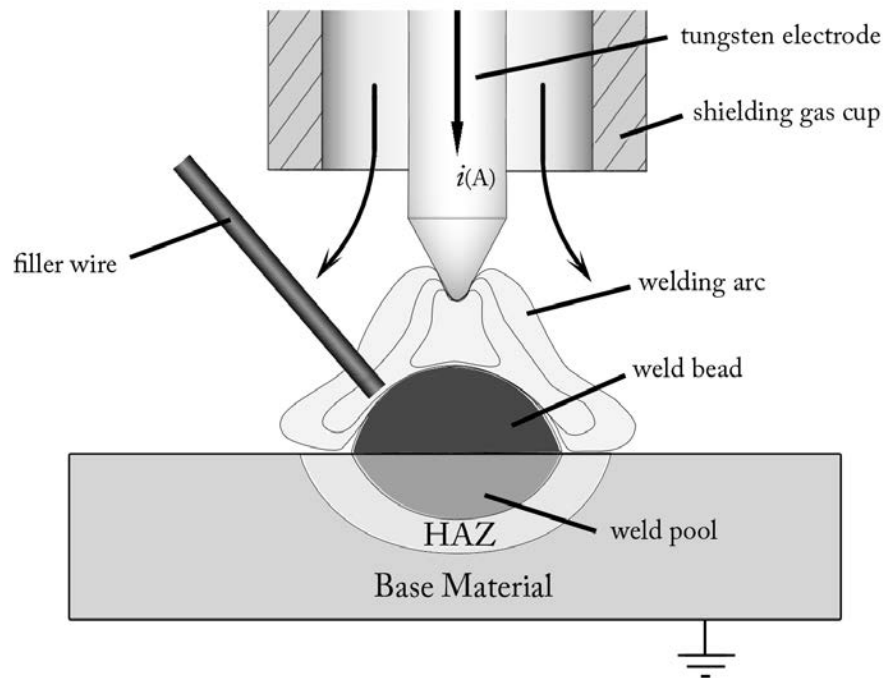


Figure 1.4: Schematic diagram of a transverse section of a cold-wire GTA weld bead

### 1.1.3 Semi-Automated GTA welding

Automating any manual process involves an understanding of the process parameters, and the human interpretation and judgement of the process. A semi-automated system has

been developed by Tool-Tec Welding in which the controllable welding parameters are set to fixed values. 3D volumes are created from 2D cross sections of horizontal surfaces as depicted in Figure 1.5, using a series of overlapping linear surface welds. This system is

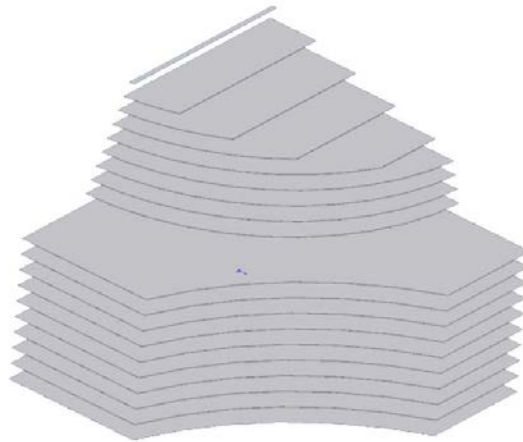


Figure 1.5: Simulation of two-dimensional weld layers that make up the final three-dimensional net shape

limited to horizontal surfaces and is not able to change process parameters in real time. Fluctuations in base temperature or base metal orientation can affect the quality and bead geometry of the weld since the controllable parameters are fixed and there is no real time feedback.

In order to fully automate the process, parameters are required to update in real-time to accommodate for changes in base metal orientation. This is done before welding begins by using a GTAW model to predict bead geometry for known base metal temperatures and orientations. During welding, the process parameters are adjusted based to correct bead geometry from changing base metal temperature.

### 1.1.4 Fully-Automated GTA welding

Investigating the effects of process parameters on weld quality and shape is one aspect of this project that is integrated with five other sections needed to create a fully automated system. The process flow is broken down into seven steps, as shown in Figure 1.6. The

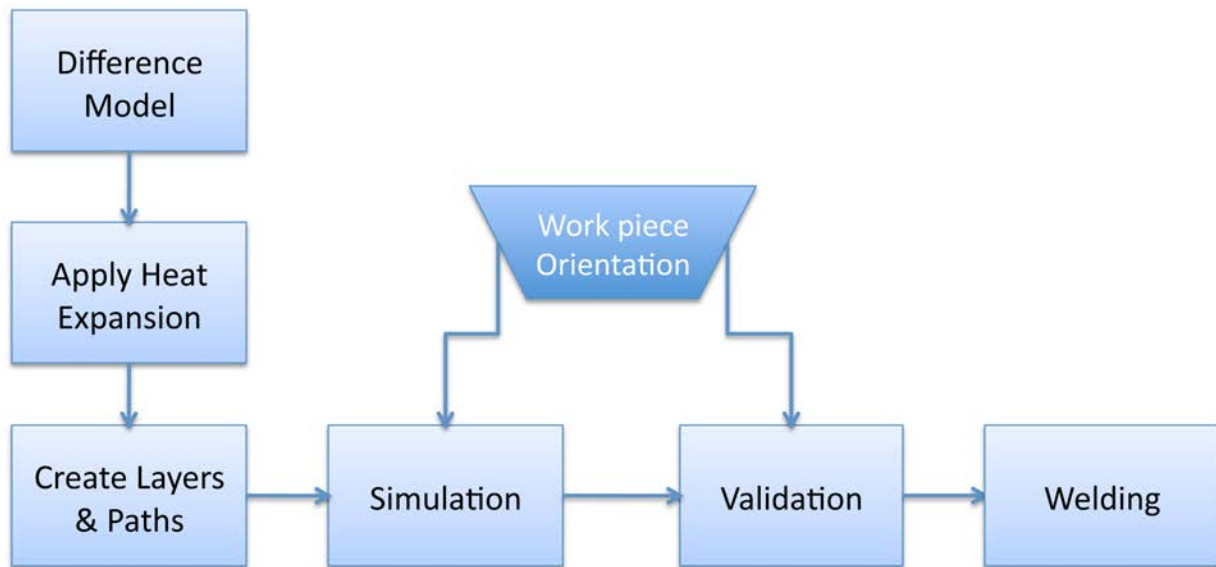


Figure 1.6: Process flow that is followed for the automated procedure, beginning with computing the CAD difference model, heat and weld path predictions, simulation, validation, and welding.

required amount of material that is to be deposited is calculated by finding the difference between the old and new mold using CAD software. Once this is computed, a theoretical heat expansion model is used to determine how the mold will expand under preheat temperatures of 500°F to 700°F. Weld paths are then generated using the 'expanded' CAD model in a CNC software package (a typical path is shown in Figure 1.7. by substituting cutter diameter by the weld pool width. These paths are then simulated in ABB RobotStudio as depicted in Figure 1.8 to avoid unexpected collisions and singularities. While the simulation is running, an operator uses a calibration end effector to detect tooling balls

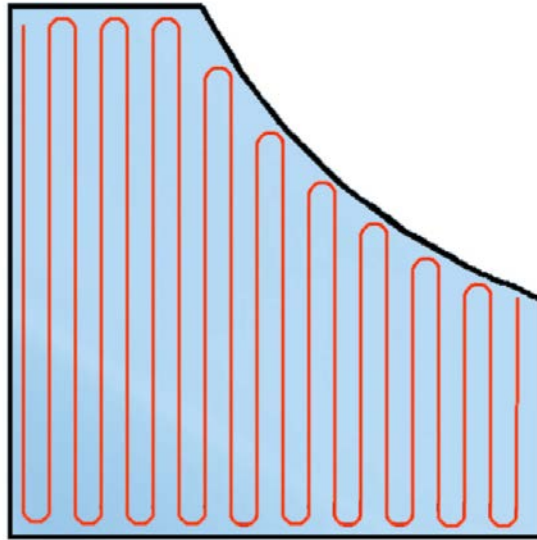
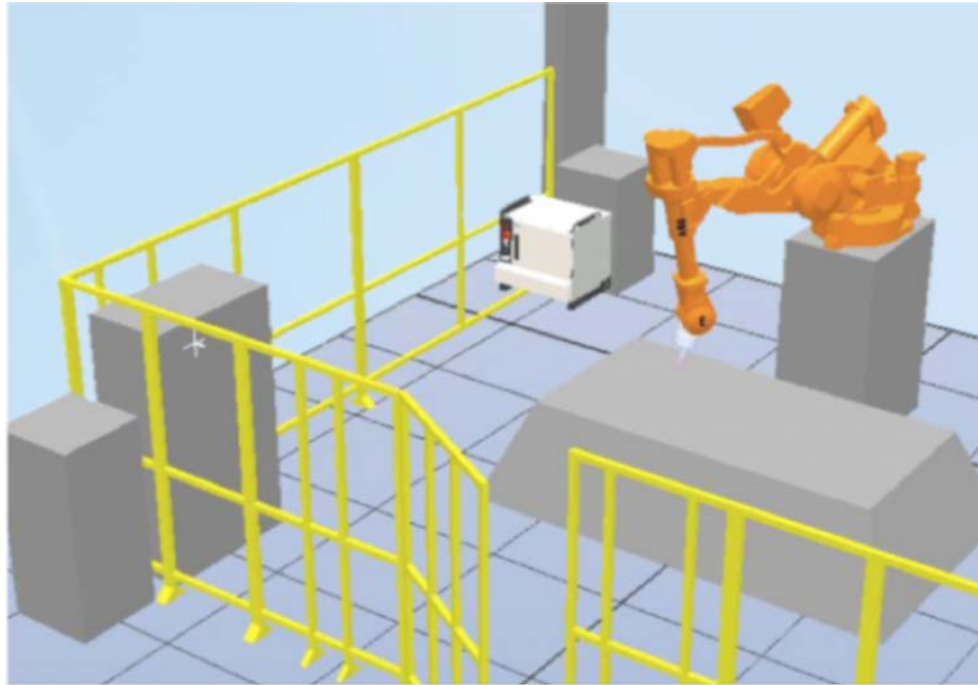


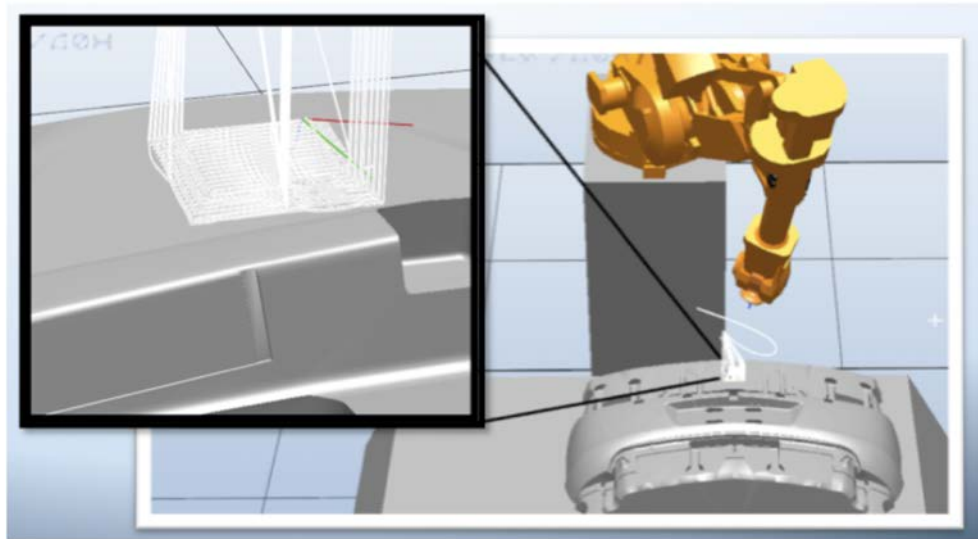
Figure 1.7: An example of a path generation using CNC software substituting cutter diameter by weld pool width for one layer of a three dimensional shape

located on the mold, which are used to determine the location and orientation of the mold with respect to the robot base frame. This is repeated after the mold is heated using a specially designed tooling ball locating sensor system. Once the heated mold location and orientation have been measured, this information is sent to the robot cell and an operator initiates the welding process.

Currently Tool-Tec only has the capability of creating a three dimensional shape by layering two dimensional layers over one another. Each layer must be horizontal so that the effect of gravity on the bead shape is constant. The CNC software, used for path generation, is limited to using one cutter size per layer. The consequence of this is that the weld bead on each layer must also have a constant width and height. A welding model is therefore needed to predict the weld bead geometry for various operating conditions and base metal orientation.



(a)



(b)

Figure 1.8: (a) Model of Robot Cell: Power Supply, Robot Controller, ABB IRB4450s, Heating table, Burner controller and PC; (b) Robot gathers joint angles by simulating paths in Robot Studio





(a)



(b)

Figure 1.9: (a) Milled and polished surface on a volume that was created using 2D software at a thickness of 1 inch; (b) 5ft long, 2D welded surface with 12 layers

Results of the two dimensional welding system are displayed in Figure 1.9(a) and Figure 1.9(b). The high quality of the welding system is verified by smooth, porous free, machined surface in Figure 1.9(a). More complicated shapes can be created from any surface shape if a welding model is developed between welding parameters and bead shape.

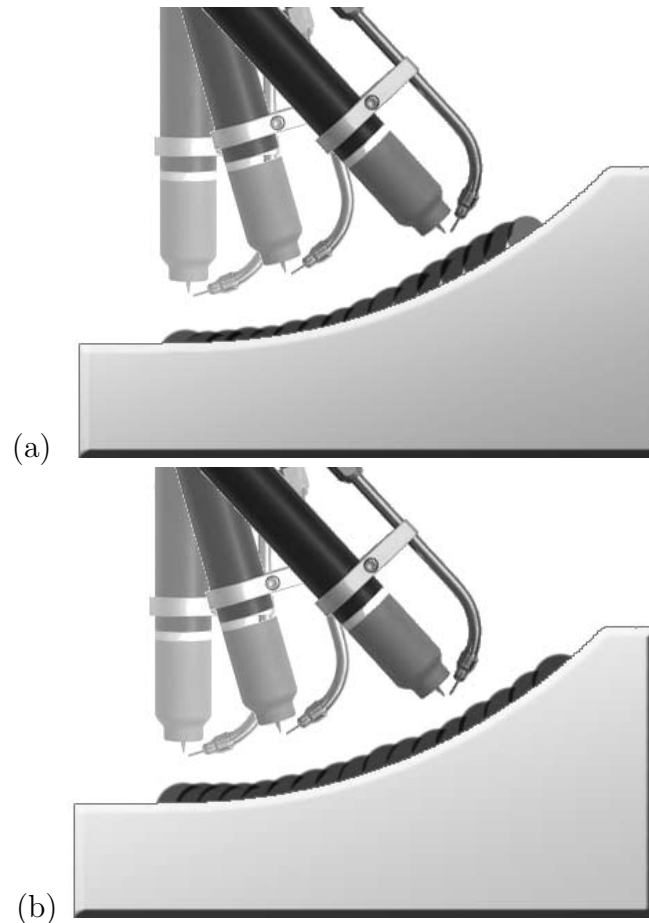


Figure 1.10: (a) effects of base metal orientation on bead geometry using fixed weld parameters (b) bead geometry effects compensated using variable weld parameters

The sensitivity of bead geometry depends greatly on changes in base metal orientation. Figure 1.10 (a) illustrates how bead height increases, for fixed set of welding parameters. Since the amount of material being deposited is constant, bead width and height have

inverse relationships to changes in base metal orientation. Figure 1.10(b) illustrates how varying GTA weld parameters during welding can be used to maintain bead geometry. Adjusting current (Amps), Travel Speed(mm/s) and Wire Feed Rate (inch/min) can achieve consistent bead geometry and good quality, however a good working model needs to be established for the parameter ranges typically used in GTAW mold repair.

## 1.2 Literature Review

The quality and mechanical properties of a weld are considered to be directly influenced by the appearance and shape of the weld [2]. Welding processes are complex due to non-linearity and coupling between process parameters. When an automated welding system is being developed, welding parameters are normally adjusted by trial and error by a skilled technician. This process is a time consuming method of determining which parameters should be chosen to achieve a desired weld characteristic. Investigating the effects of process parameters on bead geometry in GTA welding has been an area of research for many years, and has improved with advances in technology and its applications towards automation.

Analytical welding models, developed from heat and mass transfer theory, can be applied to a wide range of processes. The seminal work in this area was done by Rosenthal [3] who described the three dimensional temperature distribution due to a traveling point heat source over an semi-infinite plate. Numerical welding models [4–8] have been shown to perform well under the conditions that they are tuned to and for a specific application. These models can be used as a priori knowledge for selecting parameter ranges to efficiently run groups of welding experiments, although they cannot run fast enough for

realtime control. Research on this subject began by simplifying the analysis to separate welding models for the welding arc and weld pool behavior[9, 10]. Some models were able to predict two dimensional temperature and velocity distributions, weld bead height, width, residual stresses as well as penetration. Eventually, this work led to combined models which were then calibrated and verified by comparing the simulation results to experimental data. Empirical models are application specific, limited in their scope and require experimental data, however they are easy to work with and can be very accurate. Considering that the operating ranges for refurbishing plastic injection molds do not vary a significant amount, implementing an empirical model would be ideal for this work.

Ganjigatti *et al.* [11] investigated the relationship between process parameters and responses for MIG welding using global regression analysis and cluster-wise regression analysis. They introduce the second approach as a method of dividing the domain into a number of clusters based on their similarity; each cluster would be assigned its own set of regression equations as opposed to having a single regression equation for the whole domain (as in their first method). The input process parameters were welding speed, welding voltage, wire feed rate, gas flow rate, nozzle-to-plate distance, torch angle and the measured responses were bead height, bead width and bead penetration. They performed a two level full factorial experiment with  $2^6=64$  runs that accounted for all combinations. They reported that the performance of both approaches were comparable; however, the cluster-wise regression analysis yielded slightly better results and might take care of system dynamics more accurately since it is a local approach.

Esme *et al.* [12] have suggested using a systematic approach to constructing a mathematical model for a GTA welding process, which is as follows:(i) identify the process control variables and their upper and lower limits, (ii) identify the quality parameters, (iii)

construct mathematical models, (iv) develop a design matrix, (v) conduct experiments, (vi) obtain mathematical relationships, (vii) apply the constructed models. They demonstrated their approach by investigating the quality of bead geometry as affected by tensile load, penetration, area of penetration, heat affected zone, upper width, and upper height. They obtained an adjusted R-square value of 0.90 for their multivariate regression model and concluded that the model fit well to the observations.

Kim *et al.* [13] have established a mathematical model for the prediction of bead width, height and penetration based on arc current, welding voltage and welding speed for a robotic GMAW application. They reported that welding speed, arc current and welding voltage influence bead width, bead height and penetration. They also conducted a sensitivity analysis that showed that the change in process parameters affects the bead width and bead height more strongly than penetration.

Song *et al.* [14, 15] have developed a 3D gas metal arc welding and milling system that combines additive techniques of free-form fabrication and the accuracy of machining. This system is useful when a large volume needs to be machined or if the material is difficult to machine because of detailed features. The authors have optimized process parameters for this process which is to be used for tool and mold fabrication. They explored the effects of welding voltage, wire feed, contact tip-to-workpiece distance (CTWD) and shielding gas composition on bead geometry and weld spatter. They were able to find optimal parameter settings using the Taguchi method and reported that welding voltage and wire feed speed have greater influences on bead quality than shielding gas composition and CTWD. They also pointed out that alternating deposition direction between layers influences tensile strength significantly. Furthermore, it was mentioned that cost effectiveness of the system could be improved by increasing deposition speed and accuracy of the deposition.

Cao and Miyamoto [16] investigated the use of molten aluminum droplets deposited layer by layer to create three dimensional parts based on CAD models. Pressurized argon gas was used to eject the droplets out of the nozzle and by controlling this pressure and translating speed of the nozzle they were able to find desired operating conditions while attempting to maximize density and droplet size. Their results revealed that the difference between the fabricated objects and CAD models was 3-8 percent in length deviation and 3 percent in diagonal deviation.

Zhang *et al.* [17] developed a rapid prototyping GMAW system capable of slicing and planning CAD data to generate welding paths from CAD data to improve accuracy of the deposited part. By using a set of typical welding parameters they were able to create many small shapes with a reasonable degree of accuracy. They emphasized the importance of temperature control and its effects on the net shape by comparing a deformed thin wall of weld which had been created by depositing a path without waiting for the previous layer to cool, with one that did. The results indicate that the initial welding conditions, such as temperature, must be maintained for a set welding parameters, otherwise the bead geometry and quality will behave unexpectedly.

Atwood *et al.* [18] have developed a rapid prototyping process using laser welding called Laser Engineered Net Shaping (LENS) to fabricate metal parts from CAD solid models. A high power Nd: YAG laser is used to heat a substrate to create a molten pool into which powder is injected thus creating a desired cross sectional geometry. They were able to create shapes with a degree of accuracy similar to a rough cut injection mold as well as create intricate cooling channels within the mold as it was being created which allow for more efficient cooling. This concept cools the mold quicker in production after a plastic component has been created so the wait time between parts is shortened, thus reducing

manufacturing time and costs.

Taminger and Hafley [19] have developed an electron beam freeform fabrication process (EBF) as a rapid metal deposition process that is compatible with a variety of weldable alloys. Although their work primarily involves investigation of process parameters on macrostructural ranges they demonstrate five complex shapes that were created using this process. Shapes were created with high deposition, unsupported overhangs, varied wire feed angle, complex curvature and transitioning geometries. They conclude by stating that before this technology should be accepted for industrial applications, a deeper understanding of process parameters is needed in order to improve surface quality and minimize residual stresses for complex geometries.

This review takes into account models that have been developed to understand effects of process parameters on weld bead geometry and also covers relevant research on multi-layer welding. These cases have provided accurate results over preset assumptions and operating ranges. Many of the above approaches are unable to provide GTA welding models for P20 tool steel, or do not include base metal orientation effects on GTA welding. The research covered in this review also indicates a high level of quality for multi-layer welding, however the metal deposition rate for these processes is slow when compared to GTAW. Therefore, an accurate GTA weld geometry model is needed for the automated refurbishment and repair of plastic injection molds.

## Chapter 2

# Measurement Systems

The automated welding system that ToolTec was developing was specified to include two vision-based measurement systems. The first was to enable measurements of certain weld features to be made (similar to Image Pro Plus software, but much less comprehensive, and specific to weld bead cross sections). This was intended to be used for off-line quality control and to provide customers with the ability to refine or develop their own process schedules. The second system was to be based on a structured light height sensor (similar to commercial seam-tracking sensors, such as those made by MVS and Servo Robot) with accompanying software to measure the weld bead profile in real-time. This was to be used for control of bead geometry in the fully automated welding system, as well as for measuring the weld bead profile in the experimental work. These two systems will be described in this chapter, together with their calibration.



## **2.1 Cross-section Weld Feature Measurement System**

In this section, a vision system is presented that is capable of providing weld dimensions from digital images of a sectioned weld. The quality of the images depends highly on the etching process which is used to bring out the detail in a macroscopic image of the weld section. The process of segmenting the boundaries of the response variables (weld bead width, bead height, penetration depth, heat affected zone depth and width) viewed in the digital image will be described, as will a calibration procedure for the imaging system.

### **2.1.1 Weld sectioning and sample preparation procedure**

Preparing the welds for inspection involved destructive testing, where samples are cut from portions of weld specimens. A horizontal bandsaw was used to cut specimens and expose the cross sections of the welds. This was followed by grinding the face of the weld to reduce the rough saw cut to a more consistent flat surface for the next step of polishing. Four stages of sanding from 400 grit to 1200 grit sand paper was used to polish the surface to a mirror finish. The boundaries of interest (weld bead, penetration, HAZ) were not visible at this stage therefore the surface of the weld needs to be chemically etched to expose these regions. Etching involves exposing the polished weld cross section to an acid for 10 to 15 seconds; the acid used was Nital, which is one part nitric acid and three parts water, by volume. After etching, the weld was rinsed with distilled water and dried to reveal the weld bead penetration and HAZ boundaries. At this point the weld boundaries are clearly identified, however before any measurements can be made the imaging system must be properly calibrated along with the development of image processing code.

### 2.1.2 Calibration of Weld Imaging System

To make the calibration of the measurement system easy for future customers to undertake and/or verify, a simple procedure using a commonly available marker (a washer) was developed. A washer was chosen since these are rotationally symmetrical, and the inside diameter of the washer can easily be measured accurately (to within 0.01mm) with a digital vernier calipers. The rotational symmetry property is also useful in that positioning the marker is not important, and in that a best fit circle template match is easy to compute. Lens barreling effects (the image distortion that can occur towards the corners of images) were investigated, but were found to be inconsequential if the bead section and marker were within the centre 80% of the image. An example of an image of a weld specimen cross section with the reference marker placed on it can be viewed in Figure 2.2. The inner diameter of the marker was measured to be 3.20mm and the corresponding image dimension was computed to be 122 pixels. The actual dimensions of the weld bead and heat affected zone (in millimeters) can thus be computed by measuring their dimensions in image pixels and multiplying by  $3.2/122$ . Figure 2.3 (left) shows how the image is first thresholded to identify the washer, and then (right) how the inside hole of the washer is isolated, the diameter of which can then be unambiguously computed. Calibration was initially needed to preform the following task of image processing, which is used to remove noise from the image as well as to normalize each since there is some variation in histogram distributions from image to image. The image processing algorithms will then be able to produce repeatable results for each weld image. An example of a typical raw image is shown in Figure2.1 at 7x zoom.

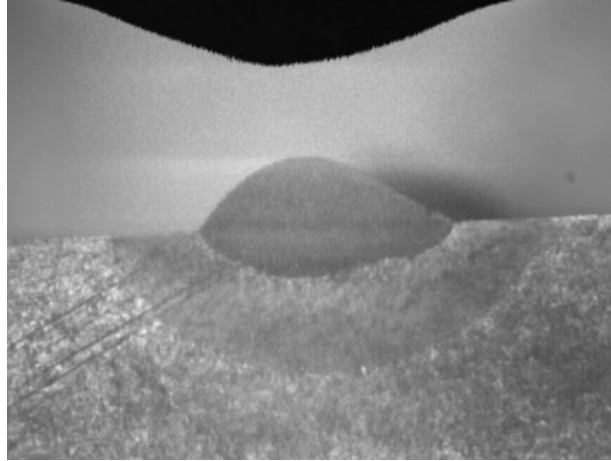


Figure 2.1: Original Image of Weld Cross-section

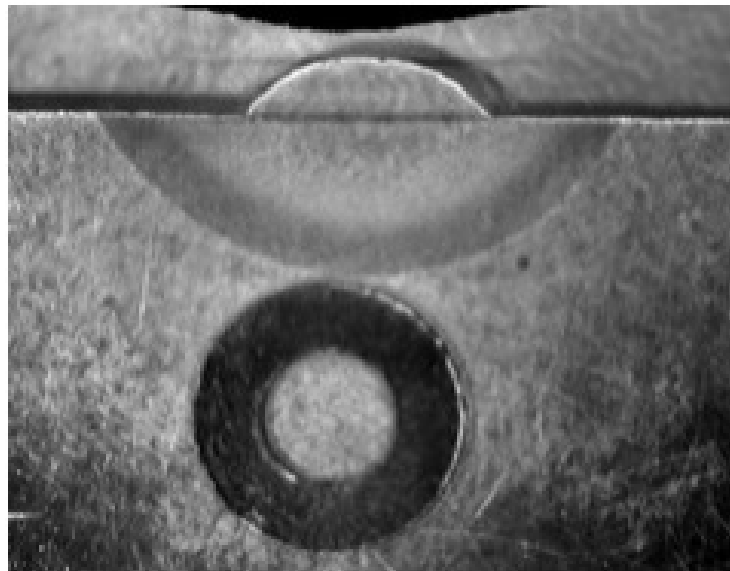


Figure 2.2: Marker on weld specimen

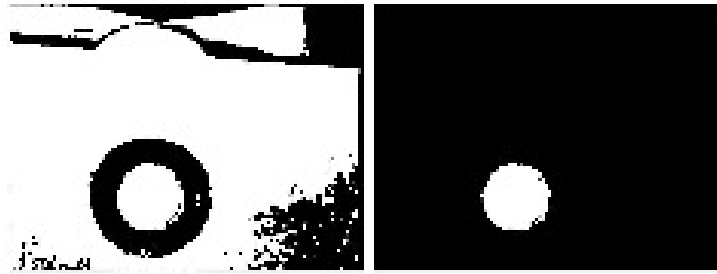


Figure 2.3: Thresholded image of marker

### 2.1.3 Image Processing for Weld Imaging System

Images were captured using a digital camera mounted on a stereo microscope with adjustable lighting. The camera was connected to a PCI frame grabber via a BNC connection. The ability to adjust the image lighting was important for maintaining the overall image exposure (or brightness), since this was found to have a significant effect on subsequent image analysis. The lighting was manually adjusted based on real-time histogram information of the image light intensity distribution for each image as shown in Figure 2.4. Controlling lighting conditions provides consistent images to be taken and reduces variation between images. The less variation that is present from image to image makes the regions of interest in the image easier to segment with the automated measurement system.

As mentioned earlier, histograms can vary from image to image but they do hold similarities. Therefore to reduce this variation histograms for each image must be normalized. The histogram for the weld images can be broken down into three sections. The background, for example, is shown in Figure 2.4 as a large spike in the 50 gray level range. The other regions of interest are within the bimodal hump in the 100-150 pixel range, which makes up the intensity distribution of the weld bead and of the base as observed in Figure 2.4.

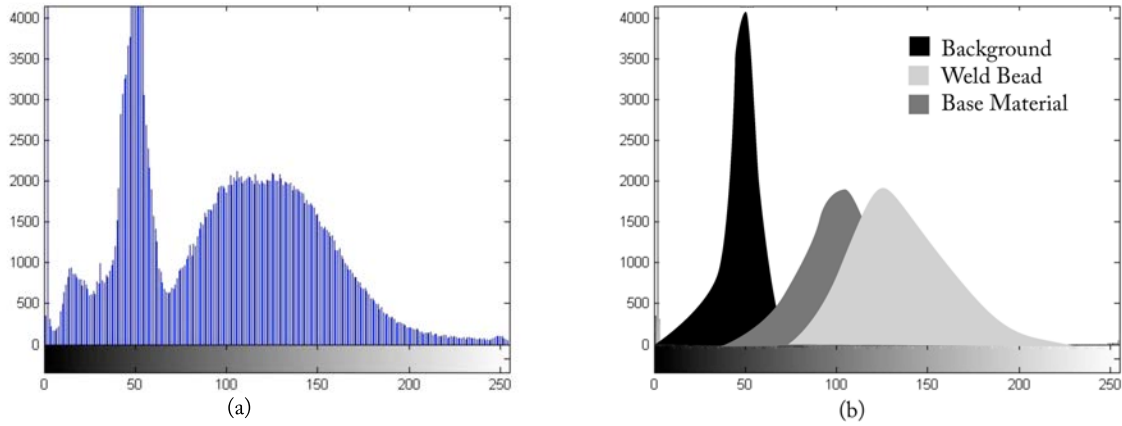


Figure 2.4: (a) Template histogram used for comparison. (b) Composition of histogram

The local minima of this bimodal hump is important to point out because to the left of this position is the background and base material and to the right is the weld gray levels. A template histogram was used to normalize each image and was created from averaging the histograms of multiple weld images. The histograms of each images were then processed and compared to the template histogram, to locate the bimodal threshold location. Thresholding the images will separate the weld from the base material. This region has a bimodal hump and is comprised of two Gaussian functions. Fuzzy logic was used to effectively increase the gap between these two Gaussian functions, which makes thresholding much easier. The fuzzy if then rules applied in this system for image processing are as follows:

1. If pixel in Background then Very Darken it
2. If pixel is Steel then Darken
3. If pixel is weld then Brighten

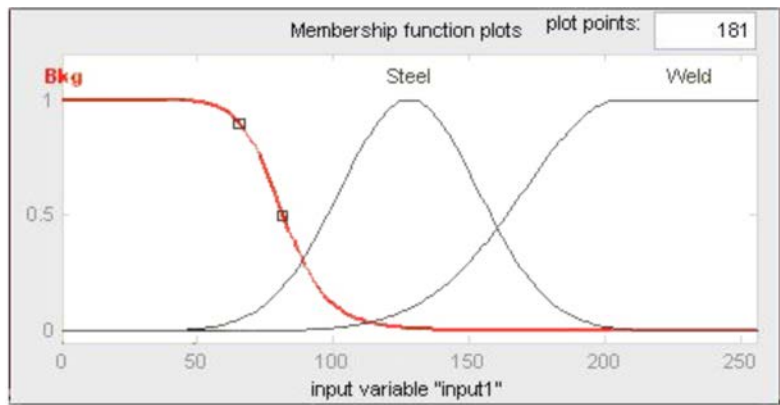


Figure 2.5: Fuzzy Input Membership Functions

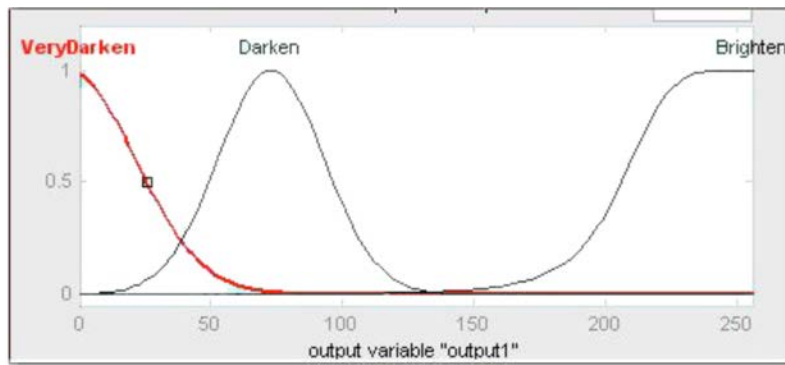


Figure 2.6: Fuzzy Output Membership Functions

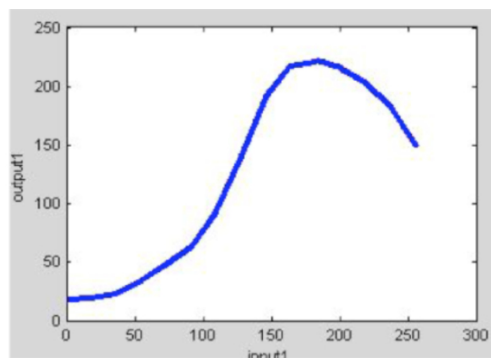


Figure 2.7: Histogram Stretching Function

The input membership functions are Gaussian and Gbell functions whose parameters are selected from image histogram and template correlation. The pixel values will be converted to a fuzzy value between 0 and 1 using the input membership functions as viewed in Figure 2.5. The fuzzy value is then used in the output membership functions as seen in Figure 2.6 resulting in the adjusted pixel value. The resulting transformation function in Figure 2.7 is used to adjust the histogram of each image where the x-axis is the grayscale value of a pixel from the original image and the y-axis is the new converted grayscale value for the adjusted image. This method of image enhancement has shifted the dark pixels and base metal to darker shades and has shifted the weld region to lighter shades. Enhancing the image before thresholding creates clearer images by increasing the contrast between the weld region and the rest of the image (background and base metal) shown in Figure 2.8a,b. After the image has been enhanced the pixel intensities are thresholded, thus creating a binary image (black and white) as shown in Figure 2.8c,d. The weld cross section can be clearly identified in Figure 2.8b, however the base material is also white and needs to be removed from the image. In order to separate the two white regions, a slight dilation of [ 5 5] window was used to make sure that the white region of the weld is to be fully enclosed by white pixels. Using preset functions in Matlab, the two white regions were labeled as 1 and 2. This was followed by applying a function that computes the compactness of each of the white regions, with the most compact shape being a circle. The weld region is always more compact than the base material region. Therefore, the region that was found to be more compact, was chosen as the the weld region and a base material region was then removed from the image. A boundary function was then used to create a perimeter around the welded region and the boundary was then superimposed onto the original image as shown in Figure 2.8e,f.

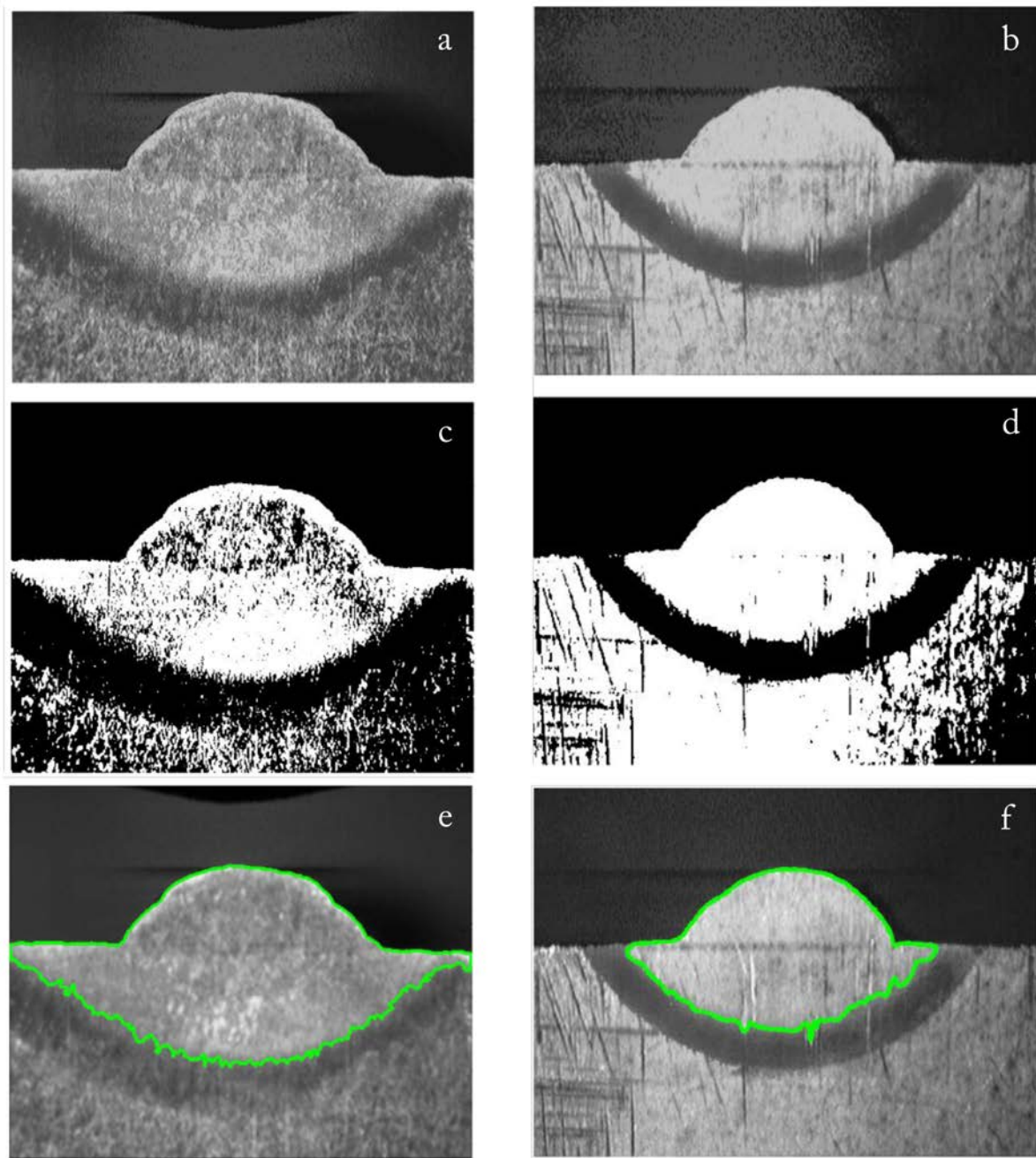


Figure 2.8: Example of Cross-section Segmentation. a) and b) Fuzzy Enhanced Images; c) and ,d) Thresholded images; e,f) Segmented Images



The resulting boundary image discussed previously now needs to be used to determine weld geometry dimensions. The boundary accurately traced the bead profile but did not trace the HAZ and penetration as well, however these two profiles can be approximated. The curvature of the penetration can be approximated to be concentric with the curvature of the heat affected zone and the intersection of a concentric circle with the weld width would illustrate the penetration profile. However, the effectiveness of this method is limited to the quality of the images and the quality of the etching process. A large degree of variation was observed between specimen images for these reasons. Thus, as an alternative to fully automating this step, the pixel locations of the image are gathered with user mouse clicks and a scaling factor will be used to convert from pixel to mm dimensions. Since only a macroscopic view of the weld is needed, less time can be spent on polishing the specimens. The accuracy of the system depends on the resolution of the images which are 640x480. This implies that 1 pixel width is 0.026mm, based on the calibration method previously described, which is more than enough for this application. This method is easy to use and is to be integrated into Tool-Tec's software for use in inspection and validation.

## **2.2 Laser Profiler**

An MVS laser-profiling camera with a field of view of 10mm was used to gather 2D profile data used for calibration and weld measurement. This unit is to be mounted on to the robot end effector used for future work involving real time weld monitoring. The profiler consists of a laser and CCD array camera that is tuned to the laser wavelength through a narrow band pass optical filter. The structured light is projected onto the surface of interest, while the sensor views the line from an angle. This allows the unit to provide

information on elevation differences as the shape of the laser line changes across various profiles. The result is similar to viewing the outer profile of the cross-section of an object. The images taken from the laser-profiling camera are sized 480x640 pixels, which are post processed in Matlab.

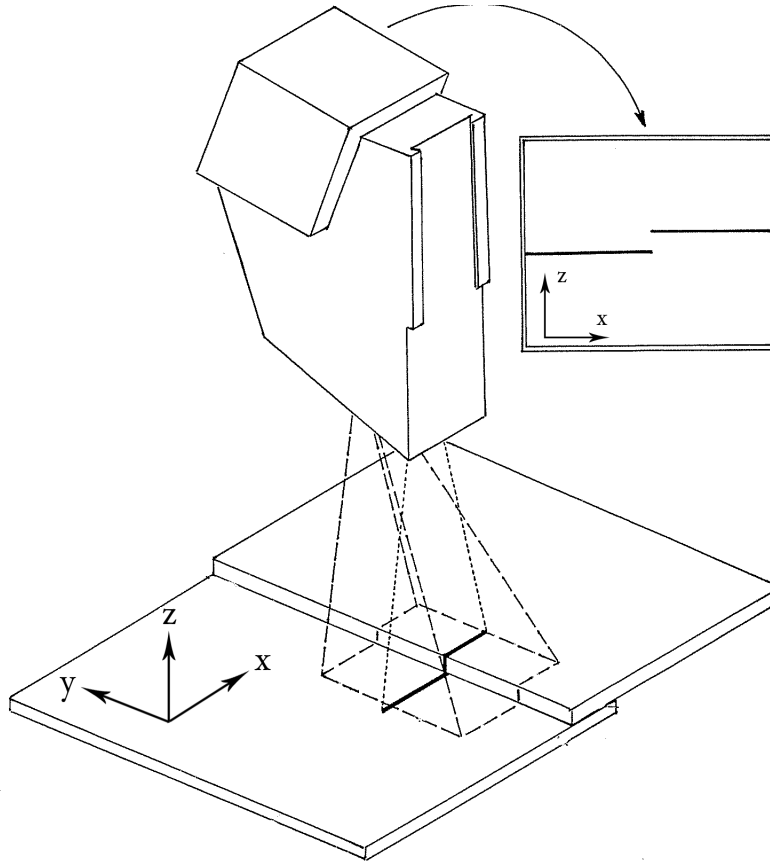


Figure 2.9: MVS Sensor

An image to world map must be created by calibrating the device in order to convert from pixel space to dimensional space. The viewing angle of the sensor (dotted line) with respect to the laser (solid line) shown in Figure 2.9, governs the aspect ratio of the image. Thus, removing noise from the image and accounting for the aspect ratio must be addressed

prior to calibration and measurement.

### 2.2.1 Image Processing of Weld Profiler

Similar to the cross section weld measurement system, image processing and calibration for the MVS laser-profiler must also be developed. Adjusting the intensity is a simple method of improving image quality, but image filtering is needed to be able to extract accurate data from the images. An averaging filter was applied to each pixel column (vertical pixels) of the image using Matlab. Filtering nearly eliminates impulsive noise, such as white specks, from the raw image. This step also normalizes the intensity distribution of the laser stripe, which looks similar to a gaussian distribution, thus making it easier to extract data from the image.

A template intensity distribution, as in Figure 2.10 (b), was used to detect the peak laser intensities by means of cross correlation. The template had a size of twenty elements in vector form. The template was compared to the first twenty elements in an pixel column, by multiplying the template values and the column value followed by summing the results. This procedure was repeated for another set that ranged from pixels 2-21, and continued until the entire column had been analyzed. The largest sum indicated the location of the peak of the intensity distribution.

The peak locations of the filtered images were assigned a value of 1 and all other pixels in that column were assigned a value of 0. This data was then used to construct a binary image depicted in Figure 2.10b. This method is effective for all cases where the intensity of the profile stripe is greatest since the profile resembles a Gaussian distribution. A comparison between the original image and the filtered image shows that the image

processing techniques used for this system are very effective for this application.

### **2.2.2 Corner Detection Weld bead**

Very small and flat weld beads are difficult to detect for the MVS laser profiler, therefore one solution to this problem is to amplify the regions where an elevation change is detected to find the edge of a weld bead. Some priori information is that the weld bead is symmetrical with the centre of the weld bead located approximately in the centre of the image. The center of the weld bead indicates the axis of symmetry which will be used as a reference location. A reference point was established by locating the peak of the bead profile and following this point down to the bottom of the image. The relative distance between each pixel location and the reference point (ref.pt, 0) provides the profile edge locations since they are closest to the reference point as shown in Figure 2.11. A new profile is created, shown in Figure 2.12, where the two smallest vertical pixel values on each side of the reference location are stored as the edge of the weld. This technique distorts the original image to further expose the edge of the weld be and was found to work very well for flat weld beads that might be a result of our experiments.

### **2.2.3 Calibration of Weld Profiler**

Effective calibration techniques were implemented to compensate for MVS sensor readings. A non-linear relationship determines the pixel to mm scaling factor that changes with pixel location. Relative distances between pixel locations were used to develop relationships. Data was gathered by moving an object with a sharp edge across the field of view of the camera by equal lateral increments. Repeating this process by vertical increments, white

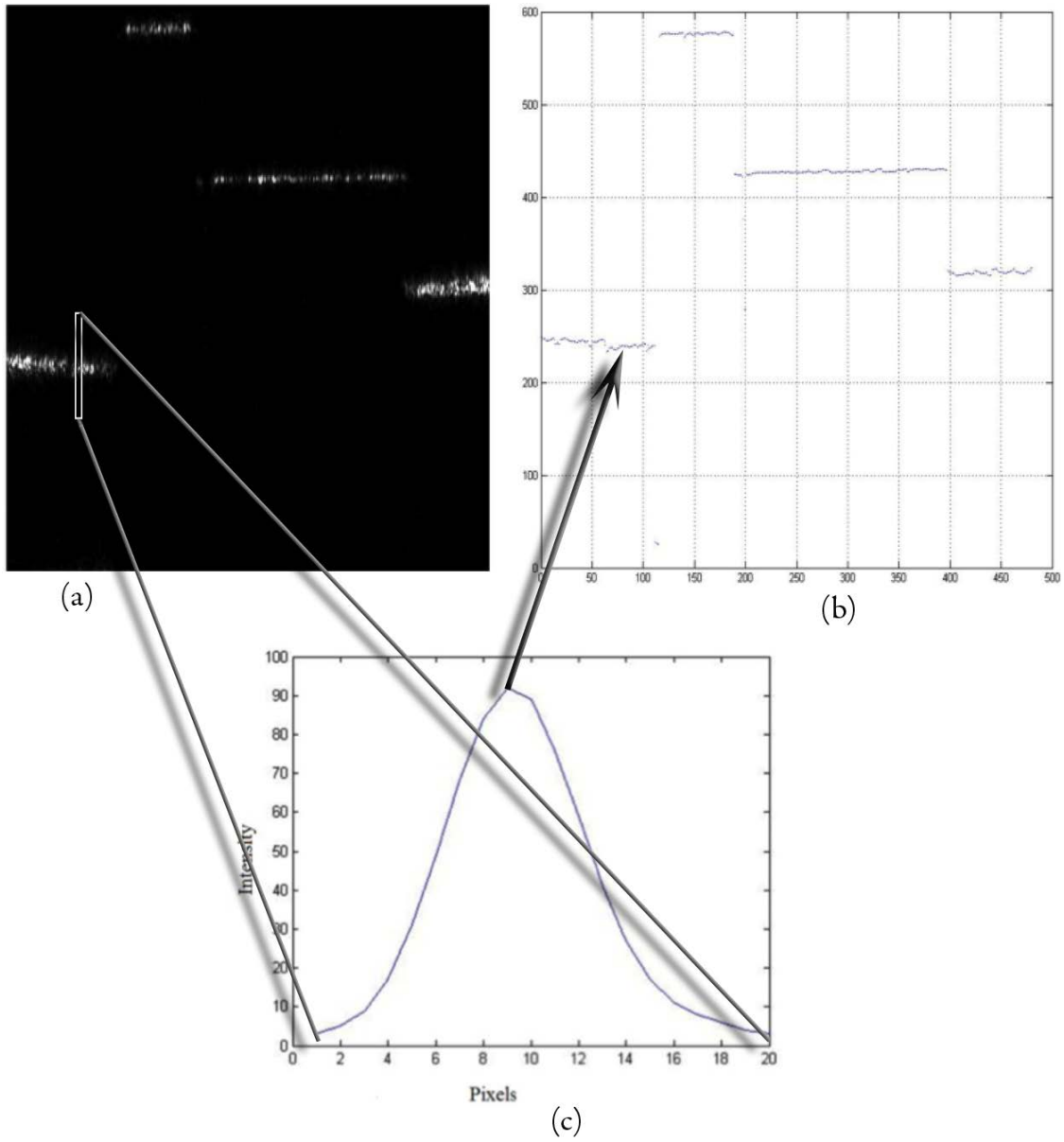


Figure 2.10: (a) original image of four gauge blocks; (b) pixel intensity distribution of laser stripe; (c) Filtered image, based on location of peak intensity of laser stripe

documenting the corner locations in real space. The cross correlation technique that was used for for the template matching section can also be used to detect edges of weld beads. The pixel locations of the filtered profile are compared in sets of ten, this time using the data from the filtered image as in Figure 2.10b. The vertical pixel locations of elements 1-10 are averaged and compared to the locations of elements 11-20. This process is repeated for elements 2-11 and 12-21, etc. until the entire row is analyzed. The greatest difference between the two averages indicate a discontinuity, which corresponds to the location of an edge as in Figure2.10b.

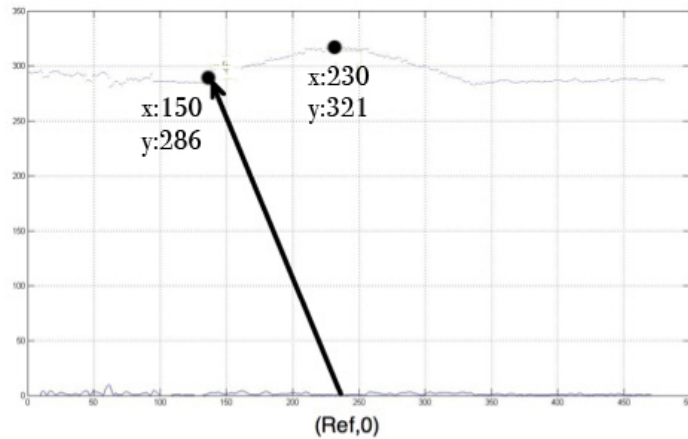


Figure 2.11: Shortest distance from reference point is edge of weld bead

## 2.2.4 Image to World Map

The relative distance between two pixel locations determines bead width and height. The conversion using the image to world map depends on where the object of interest is in the 640 range ( $z$ ). By moving an object with a sharp edge across the field of view of the camera by 0.5mm increments has provided data for direct calibration. Using the calibration data

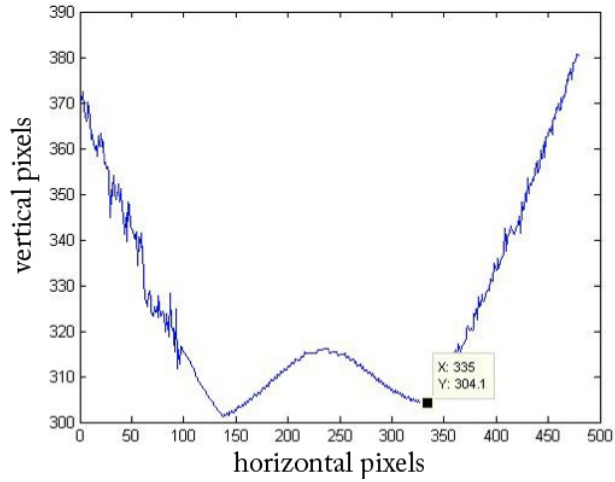


Figure 2.12: Transformed profile image provides simpler corner detection

from Figure 2.13, relationships describing the distortion in both vertical and lateral ranges were developed. The width and height of an object distorts laterally and vertically as the object is observed in various locations. The calibration data was collected and grouped into two matrices, one that contained all the z data and another that contained the y data. This provided a means of interpreting lateral and vertical distortion on both width and height.

Based on the calibration data it was found that the width and height of an object varied in pixel dimensions the further or closer the object was to the sensor. The height and width of a weld is determined by the following relationships:

$$width = \frac{pixel_w}{0.0305pixel_h + 39.0552} \quad (2.1)$$

$$height = 0.0428pixel_h - 6.5057 \quad (2.2)$$

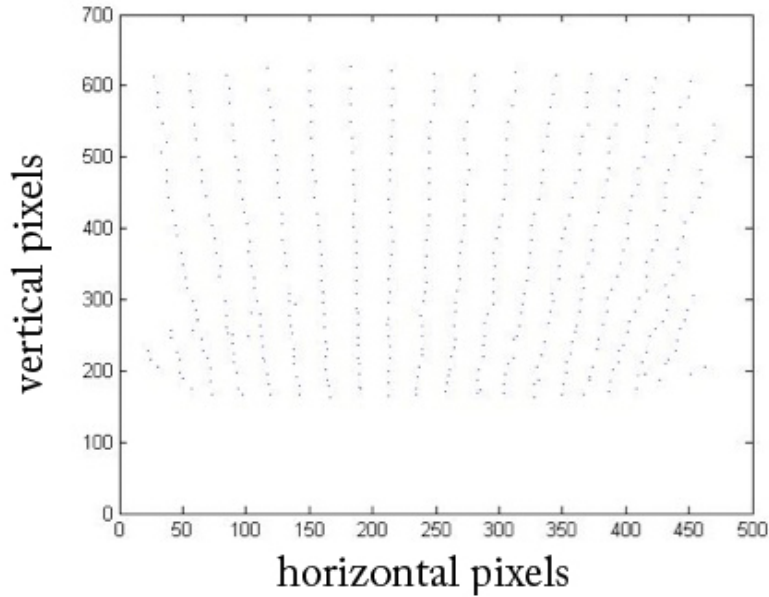


Figure 2.13: Calibration data

where  $pixel_w$  is the width of the weld in pixels,  $pix_h$  is the pixel location of the base of the weld and  $pixel_h$  is the height of the weld in pixels. These relationships produced very good results when tested by measuring gauge blocks.

### 2.2.5 Accuracy

To test the accuracy of this method, images of a gauge block of known width and height were taken in various positions in the cameras field of view. Nine images were used to measure the width of the gauge block with three near the top of the screen, three near the center of the screen, and three near the bottom of the screen. Each of the three were spaced out laterally with the second in the center of the screen and the other two adjacent to the second. Twelve images were used to measure the height of the gauge block in the same order as the width images with an additional row of images near the bottom of the



screen. The dimensions of the gauge block in the images were computed using the image to world map, and gave an average of 1.5 percent error. This means that for a typical weld of width 7mm and height of 2mm it is expected to have a measurement error of 0.10mm and 0.03mm respectively.

# Chapter 3

## Pilot Experiment and Analysis

The relationships between weld bead geometry and process parameters is complex because of the number of parameters that are involved. A general understanding of GTA welding parameters and their effects on bead geometry and quality has been developed through a literature review and discussions with skilled welding technicians. In the early stages of this research it was decided that a pilot experiment would be very useful to understand and experience the GTA welding process and common errors when performing experiments. The design, implementation and results of a pilot experiment are covered in the following section.

### 3.1 Experimental Design

The one factor at a time method for experimentation was once considered to be the correct way to conduct experiments by varying factors one at a time while the other factors are held constant. This method only provides an estimate of the effect of one factor at fixed and

selected conditions of other factors and assumes that the response acts the same when the fixed factors change. Unlike the one factor at a time design, the factorial design contains every combination of levels for the factors considered in the experiment. Factorial design using orthogonal arrays provide a quick and effective method of determining main effects when time and resources are limited. Orthogonal arrays also produce reproducible results, which are essential if the experiment is to be repeated.

The controllable parameters that were initially considered were Current (Amps), Voltage (V), Wire Feed Rate (inch/min), Robot Speed (mm/s), Temperature(degF), X-orientation (deg) and Y-orientation(deg). If a full factorial experiment were considered with two levels for each parameter then the total number of runs for the experiment would be  $2^7 = 128$  and  $3^7 = 2187$  if three levels for each parameter were considered. Ultimately, a fractional factorial design was chosen since it consists of carefully selected experimental runs of a full factorial design. They include only a fraction of the cells of a completely crossed design. The runs are chosen to expose information about the most important features of the experiment with a fraction of the effort of a full factorial experiment.

The current was held constant at 150 Amps for the pilot experiment to reduce the total number of runs in the experiment. The main reason for this is that controllable welding parameters tend to increase as current increases and thus larger values of current directly relate to large weld beads. By eliminating current as a variable the pilot experiment was simplified from 128 runs to 64 for a full factorial. This also provided an opportunity to understand how the remaining parameters affect weld quality and bead geometry. A full factorial of 64 runs was viewed as a large experiment and by using fractional factorial designs the number of runs could be further decreased. The final designed experiment employed a L27 orthogonal array with five factors as shown in Table 3.1.

Table 3.1: L27 fractional factorial pilot experiment

Run	Speed (mm/s)	Wire feed (ipm)	Stand off (Volt)	Temp (F)	x.rot (deg)	y.rot (deg)
1	1	1	1	1	1	1
2	1	1	2	2	2	2
3	1	1	3	3	3	3
4	1	2	1	2	3	2
5	1	2	2	3	3	1
6	1	2	3	1	2	1
7	1	3	1	3	3	2
8	1	3	2	1	3	1
9	1	3	3	2	1	2
10	2	1	1	2	2	3
11	2	1	2	3	1	3
12	2	1	3	1	1	2
13	2	2	1	3	1	1
14	2	2	2	1	2	2
15	2	2	3	2	3	3
16	2	3	1	1	3	2
17	2	3	2	2	1	3
18	2	3	3	3	1	2
19	3	1	1	3	2	3
20	3	1	2	1	1	3
21	3	1	3	2	2	1
22	3	2	1	1	2	3
23	3	2	2	2	3	1
24	3	2	3	3	2	1
25	3	3	1	2	1	1
26	3	3	2	3	2	2
27	3	3	3	1	3	3

Table 3.2: Parameter Levels Pilot Experiment

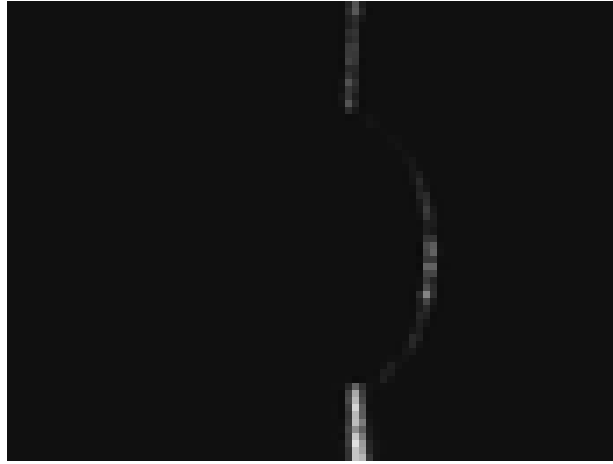
	Level 1	Level 2	Level3
A: Robot Speed (mm/s)	2	3	4
B: Wire feed (inch/min)	30	35	40
C: Voltage (V)	14	15	16
D: Base Temperature (deg F)	300	500	700
E: X orientation (deg)	0	20	40
F: Y orientation (deg)	30	0	-30

Process parameters considered are as follows: Wire feed, Robot Speed, Voltage, Base Metal Temperature, Orientation of base metal about x-axis and Orientation of base metal about y-axis. X and Y orientation refer to the rotation in degrees about an axis which dictates the orientation of the base material. X-orientation, also referred to as roll of the base material, ranges from 20 to 40 degrees. These values were chosen under the assumption that weld pool distortion is symmetrical for positive and negative degrees of roll. Y-orientation or pitch of the base metal, ranges from -30 to 30 degrees with a positive representing uphill welding and a negative value representing downhill welding.

The welding materials used for the experiment was 9210 (P20) steel for the filler wire and for the base material. A custom steel frame was constructed to mount the different the nine orientation combinations of base metal plates. Calibration of power supply and robot controller are completed on a bi-monthly basis at Tool-Tec ensuring that accurate values of current, voltage and travel speed were expected. The wire feeder was calibrated by setting a desired feed rate in inch/min and feeding the wire for one minute. Measuring how much wire was fed divided by the amount of time it took to feed determined the actual wire feed rate. During the welding process the temperature of the specimens as maintained by a hand held propane burner. An infrared temperature sensor was used to monitor the base temperature and welding commenced once the desired temperature was reached. The

Table 3.3: Measurements of L27 Experiment

Run	Width(mm)	Height(mm)
1	6.23	1.99



results of the experiments are shown in Table A.1 and Table A.2 in the Appendix. Only weld profile measurements were taken for the pilot experiment since it is assumed that penetration and HAZ geometry changes proportionally to bead geometry.

Findings from the experiment were generalized into High and Low conditions for each parameter in Table 3.4. From the experiments it was observed that travel speed, wire feed and temperature had the greatest effects on bead geometry. Increasing bead width could be accomplished by decreasing travel speed, increasing wire feed rate and temperature. Increasing bead height was achieved by increasing travel speed, wire feed and y-orientation. However, the amount of which these factors contributed to the overall bead shape or if any interactions were present was difficult to observe.

Box plots are a quick way of examining one or more sets of data graphically. The plots provide five number summaries; the smallest observation, lower quartile, median, upper

Table 3.4: Effects of high and low parameter values on nominal bead geometry

	High	Low
Robot Travel Speed	Thin and tall	Wide and slightly taller
Wire Feed Rate	Tall bead	Wide and short bead
Voltage	Small effect	Small effect
Base temperature	Small effect	Slightly wider
X Orientation	Wide bead	Small effect on bead width
Y Orientation	Tall skinny bead	Small effect on bead height

quartile, largest observation and outliers. An ideal box plot, as in Figure 3.1, is composed of normally distributed data with the size of the box indicating the distribution of fifty percent of the data about the mean. The two outer tails illustrate the distribution of the remaining data, with equal lengths for normally distributed data sets. Outliers show up as points located outside of the outer tails and do not affect the shape of the boxes.

The performance of the selection of high and low parameter levels for this experiment were examined using a box plot. Large wide boxes indicate that the response is very sensitive to the parameter levels or parameter level combinations, implying that the gap between high and low levels should be decreased. Compact boxes and tails indicate that the response is consistently influenced by parameter levels or parameter combinations with moderate variation in response. Skewed boxes indicate that the data is not normally distributed, implying that parameter levels need to be tuned to produce normally distributed data.

Figure 3.2 shows box plots for all six parameters and their contributions to weld bead width and height. The effects of increasing levels of travel speed decrease bead width Figure3.2 (a) and do not affect bead height as much Figure3.2 (g). Low levels of wire feed rate produce a variation of bead heights and widths, where as high levels have less variation in bead geometry Figure3.2 (b,h). This occurs because of the constant current value that

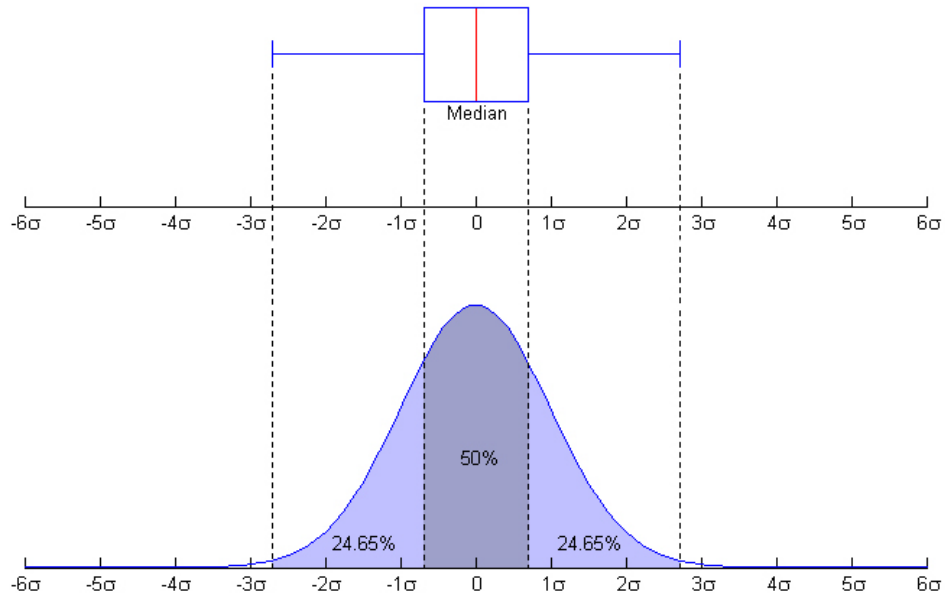


Figure 3.1: Box plot characteristics stem from normal distribution

limits the bead size from the limited amount of energy provided from the 150 amp arc. Voltage, x-orientation and y-orientation show in Figure 3.2 (c, i),(e, k),(f, l) respectively, appear to have little effect on bead geometry for fixed current values. This is expected to change for both orientation when current is increased due to the effects of gravity for a larger weld pool with increased base metal slope. The effects of temperature should be considered as a good indication of how current affects bead geometry since most of the heat is released from the arc. High levels of temperature increased bead width Figure3.2 (d) and decreased height Figure3.2 (j). Similar effects on bead width and height are expected if current were considered as a controllable parameter.

It is recommended for the full set of experiments following the pilot that current should be investigated and voltage and temperature should be removed in order to maintain a small number of runs. Temperature is removed since the nominal temperature of the base



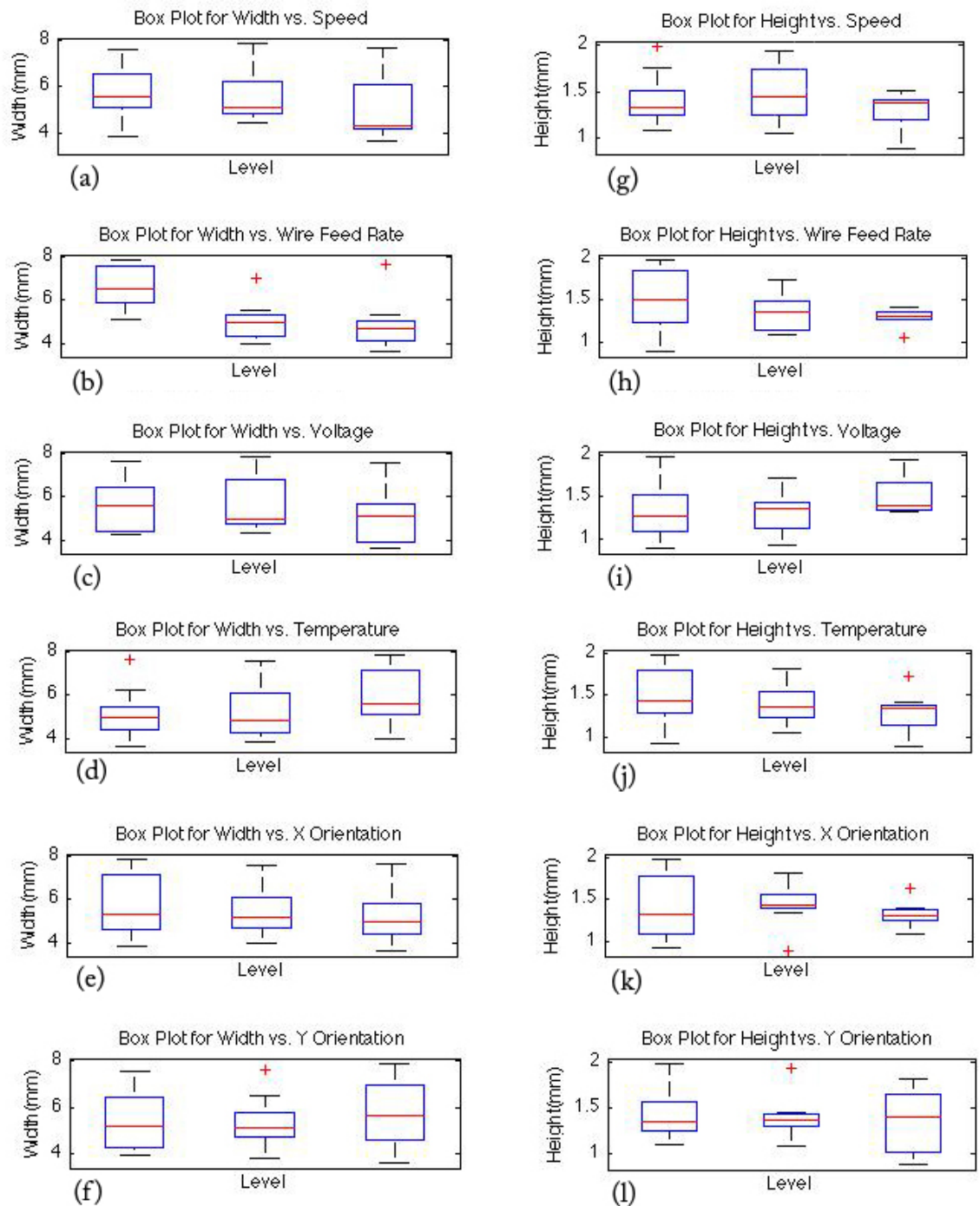


Figure 3.2: Box plots for response variables height and width and controllable variables current, voltage, wire feed rate, x orientation and y orientation

material (mold) is preheated to 500 degrees fahrenheit; therefore it is not necessary to consider other temperature ranges that are not used as often.

Overall, the pilot experiment provided a very good reference as to how the process parameters under consideration affected the bead geometry and quality of weld. The effects of current on bead geometry and its interactions with other parameters is still unknown. This experiment was carried out with current set to 150A, which is considered a smaller than average size weld beads for mold refacing. It is understood that weld size is constrained by current, therefore the next set of experiments should include larger current ranges from 200A to 300A. Since mult-layer welding for molds requires depositing a large amount of material in the shortest possible period of time, it would be more efficient to generate data that produce large welds while still maintaining weld quality.

# Chapter 4

## Main Experiments and Analysis

The results from the pilot experiment showed that weld bead, penetration and heat affected zone (HAZ) geometries are influenced by wire feed rate, travel speed, voltage, preheat temperature, and surface orientation. The pilot experiment also showed that by increasing the current and other parameters accordingly, larger welds are generally produced. The objective of the experiments described in this chapter is to quantitatively estimate the main effects of the controllable welding parameters on bead shape and size. This will be based on analysis of variance (ANOVA) of experimental results.

It was recommended by welding specialists at Tool-Tec Welding Inc., that a current range from 150 to 300 Amps should be investigated; consequently, current is introduced as a new control parameter, with a range from 200 to 300A. The Arc Height controller developed by Tool-Tec Welding Inc. was to be used to maintain a constant arc height. Since this is based on the principle that arc height (or length) is directly proportional to arc voltage for a given arc current, maintaining a constant arc length implicitly determines the arc voltage and vice versa (this is also known as Automatic Voltage Control or AVC).

The temperature factor will also be removed in these experiments since the base metal temperature used in production by Tool-Tec Welding is 500F, and significant variations from this are not allowed. It should be noted that changing the selection of controllable parameters means that the results of the pilot experiment cannot necessarily be mapped onto the results of these main experiments.

## 4.1 Parameter levels and experiment design

The parameters of interest in these experiments are:

1. Welding current(Amps)
2. Wire feed rate (inches per minute - ipm)
3. Robot (torch) travel speed (millimeters per second - mm/s)
4. Torch X-orientation (deg.)
5. Torch Y-orientation (deg.)

It was recommended by welding specialists at Tool-Tec Welding Inc., that a current range from 150 Amps to 300 Amps should be investigated (300A is the upper limit of the power supply). Since the pilot experiment had been conducted at 150A, the nominal welding current levels for these experiments were chosen as 200A and 270A, the latter being 10 percent below the upper limit to ensure the peak current (see below) stays under 300A. While it is possible to select a range for each of the other controllable welding parameters that will produce a reasonable weld bead for any combination of these parameters for a

given current, it not possible to do so for a 70A change in current. If 200A and 270A welding currents are to be evaluated, each will require different ranges of the other welding parameters, and as such, a general factorial experiment is not possible. Thus two sets of experiments are required, one for a nominal welding current of 200A and another for 270A. To investigate the effect of change in current for each nominal value, we chose to vary the current about the nominal value by  $\pm 10$  amps.

The welding power supply produces a pulsed current waveform for which the duty cycle and ratio between background current and peak current can be set, the time-average of the current being the specified current level. The power supply also synchronizes the wire feedrate to the current, and again the background and peak wire feedrates can be set. It is thus a fairly complex exercise to find a combination of duty cycle and amplitude ratio values for both current and wire feedrate such that every combination of current and wire feedrate produces a reasonable weld bead at a specified nominal travel speed. After much experimentation, for the 200A nominal welding current, a 50 percent duty cycle and amplitude ratio of 1.22 was found suitable, resulting in a background current level of 171A and peak current of 209A (average 190A) and a 50 percent duty cycle with a background current level of 189A and peak current of 231A (average 210A). Together with a nominal wire feedrate of 56 ipm 10 ipm (resulting in a low pulsed wire feedrate of 41 ipm background and 51 ipm peak, and a high pulsed wire feedrate of 59 ipm background and 73 ipm peak), all four combinations of low and high currents and wire feedrates generated acceptable welds at 4.5 ipm robot travel speed. It was found that varying the robot travel speed by 0.5 ipm provided the working envelope for the above current and wire feedrate ranges, thus completing the definition of the experimental ranges of these three parameters. The same exercise was applied to the nominal 270A welding current, and the resulting current, wire

feedrate, and robot travel speed values are as shown in Table 4.2.

The same specimen orienting fixture that was designed for the pilot experiment was used for these main experiments, and is depicted in Figure 4.1. This provides nine orientation combinations (three X and three Y orientations). All combinations of welding parameter values for both the 200A and 270A nominal welding currents produced satisfactory weld beads in all nine orientations.

Since the objective of these experiments is to estimate a first order (linear) model of the effects of the controllable parameters and their interactions on the bead shape and size, only two levels of each of the controllable parameters is required, and these were chosen as the values described above. A full factorial experiment with 5 parameters each with two levels requires 32 tests (2<sup>5</sup>), and so for the two nominal current values, a total of 64 tests would be required (without repetition). This was considered acceptable by Tool-Tec Welding. We chose to denote the experimental layout for the lower nominal welding current (200A) as Experiment A and that for the higher nominal current (270A) as Experiment B. The Low and High (denoted as - and + respectively) values for each parameter are summarized in Tables 4.1 and 4.2 for Experiments A and B respectively. The N/M notation for current and wire feedrate in these Tables refers to the peak (N) and background (M) values of each of these parameters at the Low and High levels, as described in the preceding paragraph.

Table 4.1: Parameter Levels for Experiment A

Label	Parameter	Unit	Low(-)	High(+)
i	Current	Ampere	209/171	231/189
ii	Wire Feedrate	Inches/minute	51/41	73/59
iii	Robot Speed	Millimeters/second	4	5
iv	X orientation	Degrees	20	40
v	Y orientation	Degrees	30	-30

Table 4.2: Parameter Levels for Experiment B

Label	Parameter	Unit	Low(-)	High(+)
i	Current	Ampere	273/247	294/266
ii	Wire Feedrate	Inches/minute	106/96	127/115
iii	Robot Speed	Millimeters/second	6	7
iv	X orientation	Degrees	20	40
v	Y orientation	Degrees	30	-30

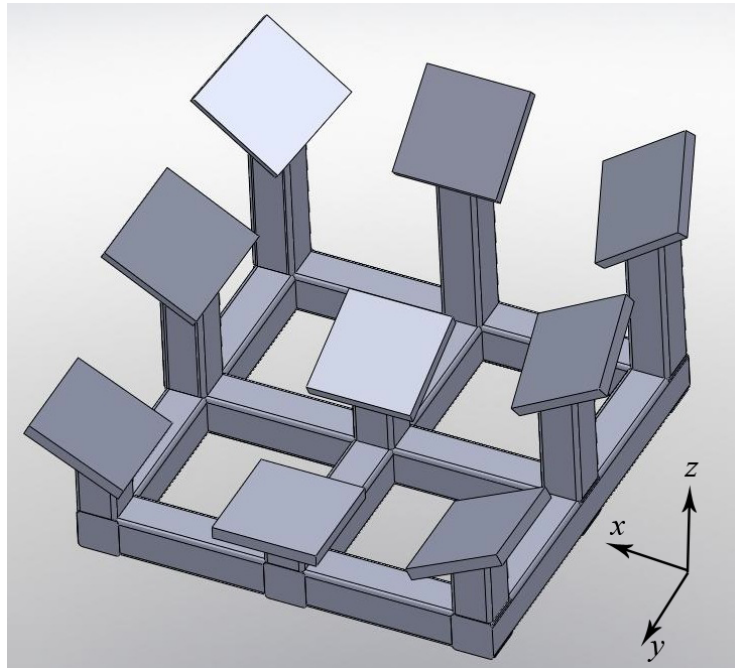


Figure 4.1: Welding fixture consisting of all x and y base metal orientations

Relative coordinate systems (work objects) were created using the ABB 4450 robot, where the tip of the tungsten was used to gently touch three points on the surface of each flat 6in x 6in x 1.5in steel specimen located on the orientation jig, to define the plane for that specimen; this was followed by creating robot positions on the specimen (robot paths). Controlling the temperature of the steel specimens before and after welding was also important for producing welds that accurately reflected the designed experiments. The temperature of the specimen was measured before each weld was made, and if this was below 450F, the specimen was re-heated using a hand-held propane burner.

## 4.2 Modeling

The GTAW process is complex and can be described by a large number of explanatory variables. Therefore, a systematic experimental process must be first defined in order to swiftly progress through problems as well as to avoid repeating errors in the experimental process. Ultimately the intention of this work is to develop a relationship between GTAW variables, namely base orientation, and weld bead shapes for P20 tool steel at 500°F. Hence, the basic steps for model-building that will be considered in this work are as follows:

1. Model Selection - Based on knowledge of welding process and assumptions of the process.
2. Model fitting - Preliminary assessment of measured responses, estimating model parameters.
3. Model Validation - Determining the plausibility of the predicted outcomes of the model using comparisons as a confirmation.



The model building processes applied in this work is displayed in a detailed flow diagram in Figure 4.2. This iterative process ensures that proper actions are taken at the end of each stage in the process. The preliminary data from the pilot experiment are now used to design new experiments, followed by measuring the responses, estimating the parameters of the model and validating the model. The process is complete once validation confirms the adequacy of the model.

The complexity of the GTAW process makes selecting the best regression model difficult because, for example, some variables might be relevant when describing bead height, but might not be relevant when describing penetration. In order to decide which variables should be included it is useful to reduce and simplify a model, to a model with less variables. However before this is done, some preliminary steps will be executed to make sure that our hypothesis will match our final results.

Variations in measured bead shapes are expected to be small, therefore it is difficult to say how significant a variable is when the changes in response vary less than 1mm between high and low variable levels. But what is certain is the relative significance of variables on a response, which can be shown graphically in a main effect plot. The main effects are calculated by subtracting the overall mean for the variable from the mean for each level. For instance, the resulting main effects of controllable variables on bead height are shown in Figure 4.3. Each level of a factor affects the response in a different way. The analysis shows that two variables, wire feed and y-orientation, contribute to an increase in bead height as wire feed is increased to a high level, while the other three variables contribute to a lower bead height as variable levels are increased. Figure4.3 also identifies the magnitude of the effect of each variable in order of significance on bead height, which are as follows: wire feed, current, robot speed, x-orientation and y-orientation. Main effect plots are useful

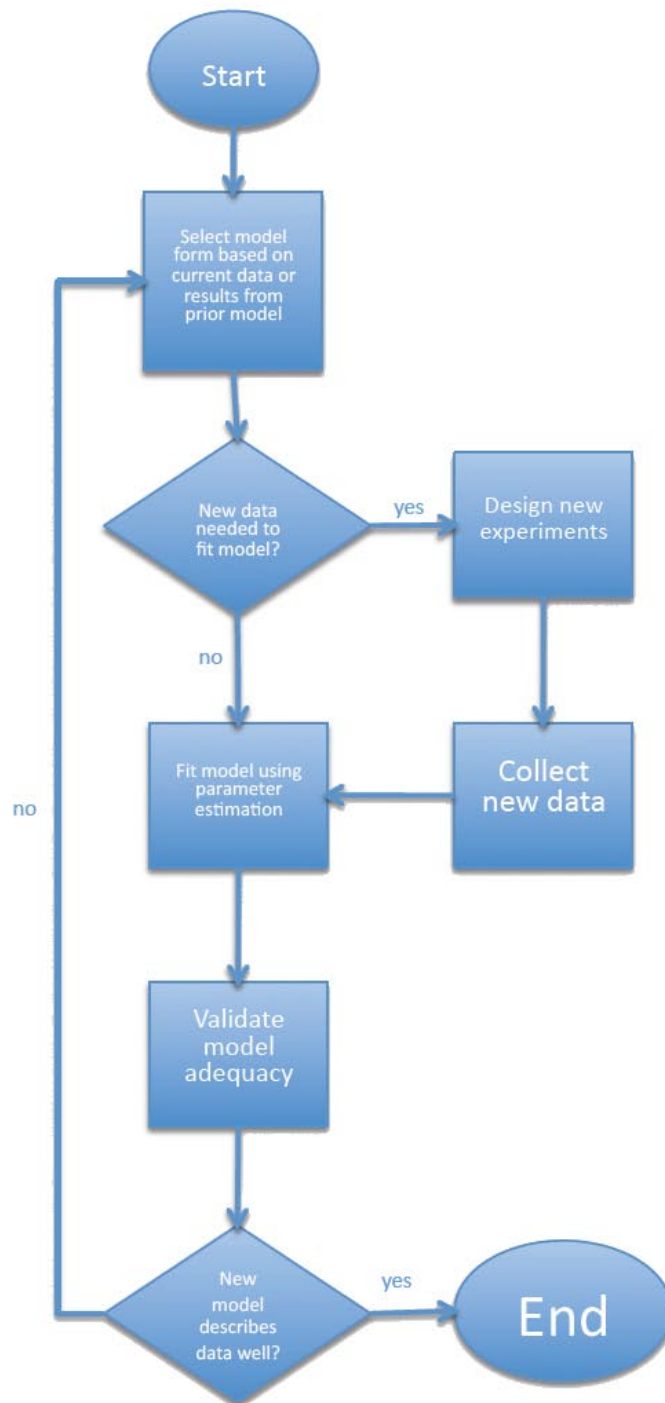


Figure 4.2: Flow chart for model fitting sequence

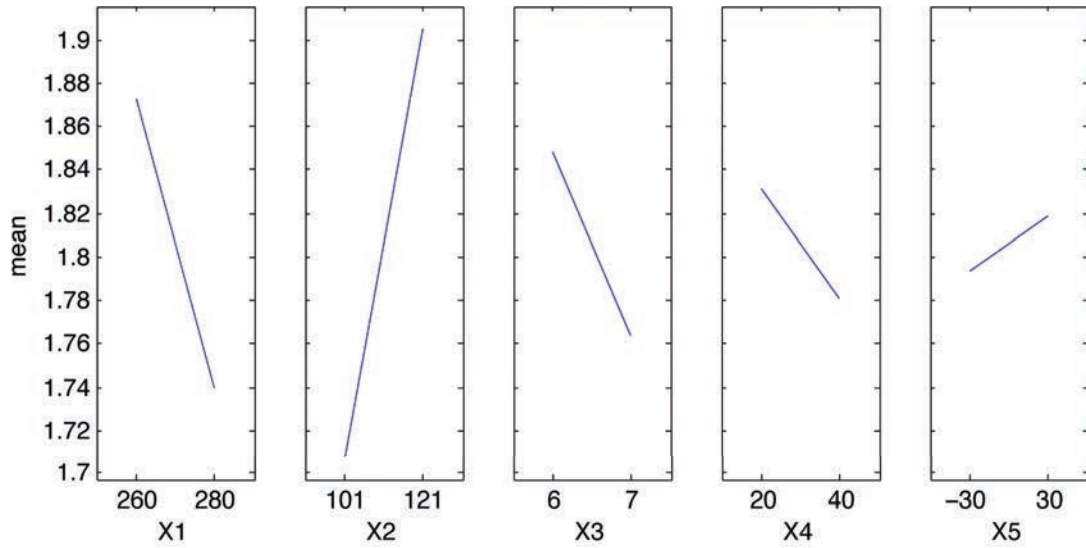


Figure 4.3: Main effects of controllable parameters on bead height, where  $x_1$ ,  $x_2$ ,  $x_3$ ,  $x_4$ ,  $x_5$  are current, wire feed, robot speed, x-orientation and y-orientation respectively

in visualizing a factors effect on a response. These plots also help during the initial stages of experimentation in that they can give hints towards which variables an experimenter should focus on more than others. Nevertheless, a proper statistical analysis is needed in order to determine which variables significantly contribute to variations in response.

The experimental data was analyzed to identify which variables significantly contribute to changes in the measured responses. This can be accomplished by using the Analysis of Variance (ANOVA) method. ANOVA is used as a method of analyzing the measured data to understand which variables and interactions are significant to response characteristics, and is described in the next section.

### 4.3 Analysis of Variance (ANOVA)

The main objective of ANOVA is to extract how much variation each factor causes relative to the total observed variation in the result. The variation caused by a single factor was considered as a percentage of the total variation. The variance ratio (F) is the ratio of the mean square due to a factor and the mean square error. A large value of F implies that the effect of that factor is more influential the variable is to the measured response. The values of the F ratio should also reflect the results of the main effects plot in Figure 4.3. A linear model was then fit to correlate response relationships based on the significant variable and/or variable interactions from the ANOVA. The table of Analysis of Variance is given in Table 4.3.

Table 4.3: Analysis of Variance Table

Variation	Sum of Squares	Degrees of Freedom	Mean Square	F
Model	SSAK	K-1	MSA	MSA/MSE
Error	SSE	K(n-1)	MSE	
Total	SST	Kn-1	MST	

where,

$$SSA = \frac{1}{n} \sum_{i=1}^k \left( \sum_{j=1}^n y_{ij} \right)^2 - \frac{1}{Kn} \left( \sum_{i=1}^k \sum_{j=1}^n y_{ij} \right)^2 \quad (4.1)$$

$$SSE = \sum_{i=1}^k \sum_{j=1}^n (y_{ij} - \bar{y}_i)^2 = SST - SSA \quad (4.2)$$

$$SST = \sum_{i=1}^K \sum_{j=1}^n (y_{ij} - \bar{y})^2 \quad (4.3)$$

$$MSA = \frac{SSE}{K(n-1)} \quad (4.4)$$

$$MSE = \frac{SSE}{K(n-1)} \quad (4.5)$$

$$MST = \frac{SST}{Kn-1} \quad (4.6)$$

$$F = \frac{MSA}{MSE} \quad (4.7)$$

A set of regression equations were fit to the measured response data to establish a relationship between weld geometry and control parameters that is to be used for the multi-layer GTA welding system. The form of the full model is as follows:

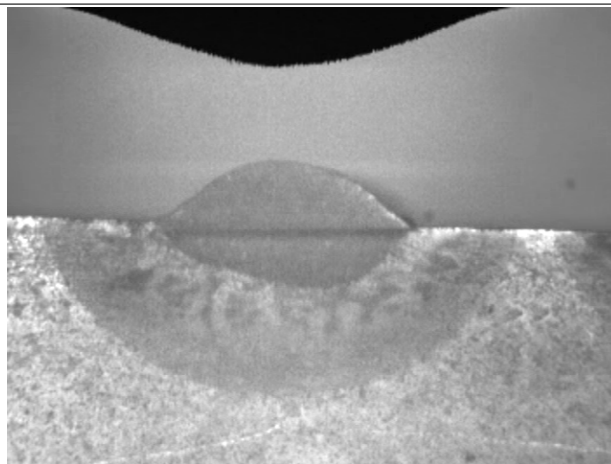
$$y = X\beta + e \quad (4.8)$$

Where  $y$  represents a measured response variable (bead height, bead width, etc.),  $X$  represents the vector of parameters  $x_1, x_2, x_3, x_4, x_5$  and their two-level interactions,  $x_1x_2, x_1x_3, \dots, x_4x_5$ ,  $\beta$  is the vector of regression coefficients, and  $e$  is the pooled error of the model. In these models,  $x_1, x_2, x_3, x_4$ , and  $x_5$  represent current, robot speed, wire feed rate, x orientation and y orientation respectively.

Similar to the the pilot experiment, the runs for this experiment were performed in a random order. Randomization allowed for other parameters that were not included in the experiment to be pooled into the error term of the analysis. Table 4.4 shows the cross-

Table 4.4: Experiment B Results

Run	Bead Height (mm)	Bead Width (mm)	Pen Depth (mm)	HAZ Depth (mm)	HAZ Width (mm)
12	1.93	7.67	1.97	5.11	14.91



section image of a weld number 12 as well as the measured responses. The response data is displayed in this format to make visual comparisons between experimental runs.

The remainder of the measured results of Experiment A are shown in the Appendix under Table A.4 and Table A.5. The measured responses for experiment B are shown in Tables A.6,A.7, also located in the Appendix. Due to the variation in pulsed GTA weld geometry, multiple measurements of the weld profile were taken to ensure the reliability of the measured data. The number of sample measurements needed for each weld was performed by randomly selecting four sections of one weld. In order to confirm that four measurements were sufficient, the residuals were plotted on a normal probability plot to show that the error is randomly distributed, meaning that four samples are sufficient. The normal probability plots are shown in Figures B to B in Appendix A.

The following sections discuss the effects of GTAW parameters on the five measured

responses based on the  $L_{32}$  experiments. A comparison are also discussed between initial assumptions and results from the pilot experiment with the results from the  $L_{32}$  experiments.

## 4.4 Results

Multi-layer welding requires a good understanding of how the shape of a weld will behave under specific conditions. This is mainly a large concern because of how each welding layer is predetermined using CNC software. The net solid volume is sectioned into layers equally spaced, therefore the weld bead height is expected to remain consistent, otherwise the net shape will have too much or not enough weld after completing the final weld layer.

The pilot experiment indicated that bead height was significantly affected by wire feed, robot speed, and y-orientation. Higher levels of current and robot speed were assumed to decrease bead height along with low levels of wire feed and y-orientation. Weld bead height was also found to show the most variation due to the pulsing of high and low current values. For this reason nominal bead heights are used for analysis.

### 4.4.1 Weld Bead Height

The Experiment A (low current range) ANOVA results for bead height are shown in Appendix under Table C.1. The table indicates that travel speed, with a p value of 0.004, is the leading contributor to variation in bead height. Increasing travel speed is expected to decrease the overall cross sectional area of the weld, therefore decreasing bead height. Wire feed, current and y-orientation, the three other factors expected to contribute to variation in bead height, were found to be considerably less critical than expected. However

the interaction between wire feed and y-orientation is shown to to be the second largest contributor to variations in bead height.

In Experiment B, a higher current range was investigated in order to broaden the range of bead geometries available. Table C.2 shows that the main contributor to variations in bead hight is the interaction of the Current and Wire feed factors. This is interesting to note because this interaction was found to be the 6th largest contributor in under lower current values in Experiment A. The other factors that significantly affected bead height are Current\*Y-orientation interaction followed by travel speed. The following linear models were fitted to the data from Experiment A and Experiment B.

Variations in weld bead height are measured in real-time by the arc length controller developed by Tool-Tec Inc.. This controller maintains a consistent arc length, which directly maintains the CTWD (contact tip to work distance). Using the feedback information from the robot controller, variations in weld bead height can be compensated by changing the target bead height for each successive layer.

#### **4.4.2 Weld Bead Width**

From the pilot experiment, it was found that weld bead width is mostly affected by wire feed rate, travel speed and x-orientation. Similar as in the case of bead height, wire feed rate and travel speed are the main drivers that change the cross sectional area. The ANOVA for Experiment A Table C.3, indicates that weld bead width is largely affected by Wire feed rate, current, travel speed and y-orientation. The other contributing factors are speed\*y-orientation interaction, x-orientation\*y-orientation interaction followed by current\*wire interaction and wire\*x-orientation interaction. Experiment B ANOVA shown in



Table C.4 shows that current is now the largest contributor in bead width variation, but its contribution, along with the remaining factors, is not apparent as it was in experiment A. Following current, the largest contributors are y-orientation, current\*y-orientation interaction, wire\*y-orientation interaction and current\*x-orientation interaction. The following linear relationships describe bead width as a function of the controllable parameters and their interactions.

For the application of multi-layer welding, the robot paths or bead width is also pre-determined using CNC software. Variations in bead width will directly contribute to bead height as excess weld will overlap adjacent welds. However changes in bead height, and indirectly bead width, can be compensated on a layer by layer basis by the Tool-Tec Inc. CTWD controller.

### 4.4.3 Weld Bead Penetration

From the pilot experiments it was expected that penetration depth would be related to bead height and width, under the generalization that tall skinny bead would imply poor penetration. As previously mentioned, tall and skinny beads can be created by increasing wire feed, increasing y-orientation, increasing travel speed, or decreasing current.

Table C.5 shows the ANOVA table for Experiment A, where the most significant factor is the wire\*y-orientation interaction. The significance of wire feed and y-orientation individually is very small, however together they can produce extreme results. While weld pool surface tension maintains continuous contact with the base material at steep inclines or declines, the gravitational effects on the weld pool force the pool downhill. Wire feed rate complements the direction of the gravitational effects.

Consider the extreme case, first where the energy emitted from the arc hardly melts the base material and solely melts the filler material. In this situation wire feed solely affects‘

Secondly, where the energy emitted from the arc is very high and melts a substantial amount of base material with the melted filler wire broadly spreading across the weld pool.

marginally followed by travel speed The remaining factors are not nearly significant enough to mention. It is interesting to note that when welding under steep base metal orientations, the weld pool tends to want to roll down the base metal. Wire feed, y-orientation and speed are shown to reduce weld pool stability as gravitational effects are increasingly predominant.

Table C.6 displays the ANOVA results for Experiment B, where in this case the most significant factors are y-orientation followed by current\*x-orientation interaction, speed\*x-orientation interaction, current and slightly speed\*y-orientation interaction. Wire\*y-orientation interaction was the main driver in Experiment A, where it is hardly considered as a significant factor in Experiment B. The effects of current from low to high ranges are obvious when observing the contribution of factors on penetration variation between Experiment A and Experiment B.

#### **4.4.4 Weld Heat Affected Zone (HAZ) Depth**

The relationship between the welding parameters and the size of the heat affected zone is not as apparent as they were for bead height, width and penetration. It was hypothesized that the heat affected zone size is directly proportional to the amount of heat dissipated into the base material ie. the amount of current, minus the amount of filler wire per unit length of weld as well as the travel speed.

From Experiment A it was found that the most significant parameters contributing to variation in HAZ depth are current\*x-orientation interaction, followed by wire\*y-orientation interaction. Experiment B showed that wire\*speed interaction is the strongest significant contributor to HAZ depth. This relationship relates to the amount of heat dissipated into the base material per unit length of weld. A slow speed weld with less filler wire will create a deep HAZ, because most of the energy is being absorbed by the base material. Conversely, a high welding speed with high filler wire rate will allow for less time, per unit length, for heat to dissipate to the base material, with a significant amount of energy going into melting of the filler wire, thus producing a short HAZ depth.

#### **4.4.5 Weld Heat Affected Zone (HAZ) Width**

Similar to HAZ depth, the effects of welding parameters on HAZ width is expected to be primarily driven by current minus wire feed and robot speed since current is related to how much energy is emitted from the arc, and wire feed and robot speed absorb this energy for a unit length of weld. The remaining heat is then transferred into the base material, for a certain arc efficiency, thus producing the HAZ.

The ANOVA table for HAZ width experiment A, shown in Table C.11, shows that the current\*x-orientation interaction is predominant in contributing to variation in HAZ width as it was for HAZ depth. Experiment B shows that the wire\*speed interaction is the most significant variable, as it was for HAZ depth, followed by wire\*y-orientation. Wire feed rate however is shown to be more significant in experiment B for HAZ width than it was for HAZ depth, since the heat emitted from the arc transfers easily across the base material compared into transferring deeply direct into the material.

The importance of HAZ size is stressed when welding on or near a class A regions on plastic injections moulds. If too large, the HAZ will be visible on the finalized machined class A surface thereby producing shadow lines on the mould which will transfer to the plastic component during production. Therefore, this application requires the ability to predict bead geometry as well as HAZ when welding near or on top of class A surfaces.

## 4.5 Reduced Models

The coefficient of determination or  $R^2$  is an indicator of how well the model fits the data. The value of  $R^2$  is between 0 and 1, and the closer  $R^2$  is to 1 the better the model fits to the data. However, a  $R^2$  value close to one can also be achieved by increasing the order of the model or by including too many variables and interactions. This type of model lacks accuracy when attempting to predict responses between the fitted data set. An over fitted model is difficult to spot when using  $R^2$  as a model performance indicator. Another indicator of how well a model fits to data is the adjusted  $R^2$ , which is a refinement to  $R^2$  that adjust for the number of explanatory terms in a model. This is useful when attempting to reduce a model by removing insignificant variables. Unlike  $R^2$ , adjusted  $R^2$  increases only if a new term improves the model, and will always be less than or equal to  $R^2$ . Therefore, if a model contains a  $R^2$  value of close to but has a low adjusted  $R^2$  value, the model will need to be reduced because it is over fitting the data.

The adjusted  $R^2$  are initially computed for the maximum model followed by iteratively reducing the maximum model according to the significance of each variable found in the ANOVA analysis. The least significant variable or interaction are removed from the model, and its contribution are pooled in the model error. The  $R^2$  and adjusted  $R^2$  are

computed once again until they are both maximized, indicating the best model describing the response.

In the following tables  $x1, x2, x3, x4, x5$  represent Current (Amp), Wire Feed Rate(Inch/min), Travel Speed(mm/s), X-orientation (degrees) and Y-orientation (degrees) respectively. The ANOVA tables 4.5 to 4.11 are shown to demonstrate how insignificant factors and interactions are eliminated in the model reduction process. The main objective is to increase adjusted  $R^2$  without significantly reducing  $R^2$ .

Table 4.5: Initial Bead Height ANOVA Table

Source	Sum Sq.	d.f.	Mean Sq.	F	Prob>F
X1	0.025	1	0.025	1.072	0.316
X2	0.066	1	0.066	2.765	0.116
X3	0.181	1	0.181	7.643	0.014
X4	0.232	1	0.232	9.76	0.007
X5	0.05	1	0.05	2.098	0.167
X1*X2	0.036	1	0.036	1.512	0.237
X1*X3	0.008	1	0.008	0.344	0.565
X1*X4	0.001	1	0.001	0.026	<b>0.875</b>
X1*X5	0.005	1	0.005	0.21	0.653
X2*X3	0.168	1	0.168	7.095	0.017
X2*X4	0.164	1	0.164	6.916	0.018
X2*X5	0.009	1	0.009	0.4	0.536
X3*X4	0.012	1	0.012	0.521	0.481
X3*X5	0.079	1	0.079	3.336	0.087
X4*X5	0.025	1	0.025	1.069	0.317
Error	0.38	16	0.024	□	□
Total	1.441	31	□	□	□

Table 4.12 shows the results of the iterative model reduction process and indicates that the 5th iteration produced a model with the largest adjusted  $R^2$  value of 0.5915, an  $R^2$  of 0.71 which is not much smaller than the original of 0.735. Also, the lowest p-value of the reduced model is of the 5th iteration at 0.0003, indicating that the model describes the data very well.

Table 4.6: Bead Height ANOVA Table; Removal of X1\*X4

Source	Sum Sq.	d.f.	Mean Sq.	F	Prob>F
X1	0.025	1	0.025	1.137	0.301
X2	0.066	1	0.066	2.933	0.105
X3	0.181	1	0.181	8.108	0.011
X4	0.232	1	0.232	10.354	0.005
X5	0.05	1	0.05	2.225	0.154
X1*X2	0.036	1	0.036	1.604	0.222
X1*X3	0.008	1	0.008	0.365	0.554
X1*X5	0.005	1	0.005	0.223	<b>0.643</b>
X2*X3	0.168	1	0.168	7.526	0.014
X2*X4	0.164	1	0.164	7.337	0.015
X2*X5	0.009	1	0.009	0.425	0.523
X3*X4	0.012	1	0.012	0.552	0.467
X3*X5	0.079	1	0.079	3.539	0.077
X4*X5	0.025	1	0.025	1.134	0.302
Error	0.38	17	0.022	□	□
Total	1.441	31	□	□	□

Table 4.7: Bead Height ANOVA Table; Removal of X1\*X5

Source	Sum Sq.	d.f.	Mean Sq.	F	Prob>F
X1	0.025	1	0.025	1.188	0.29
X2	0.066	1	0.066	3.065	0.097
X3	0.181	1	0.181	8.474	0.009
X4	0.232	1	0.232	10.821	0.004
X5	0.05	1	0.05	2.326	0.145
X1*X2	0.036	1	0.036	1.676	0.212
X1*X3	0.008	1	0.008	0.382	<b>0.544</b>
X2*X3	0.168	1	0.168	7.866	0.012
X2*X4	0.164	1	0.164	7.668	0.013
X2*X5	0.009	1	0.009	0.444	0.514
X3*X4	0.012	1	0.012	0.577	0.457
X3*X5	0.079	1	0.079	3.698	0.07
X4*X5	0.025	1	0.025	1.185	0.291
Error	0.385	18	0.021	□	□
Total	1.441	31	□	□	□

Table 4.8: Bead Height ANOVA Table;Removal of X1\*X3

Source	Sum Sq.	d.f.	Mean Sq.	F	Prob>F
X1	0.025	1	0.025	1.228	0.282
X2	0.066	1	0.066	3.168	0.091
X3	0.181	1	0.181	8.759	0.008
X4	0.232	1	0.232	11.185	0.003
X5	0.05	1	0.05	2.404	0.138
X1*X2	0.036	1	0.036	1.733	0.204
X2*X3	0.168	1	0.168	8.13	0.01
X2*X4	0.164	1	0.164	7.926	0.011
X2*X5	0.009	1	0.009	0.459	<b>0.506</b>
X3*X4	0.012	1	0.012	0.597	0.449
X3*X5	0.079	1	0.079	3.823	0.065
X4*X5	0.025	1	0.025	1.225	0.282
Error	0.393	19	0.021	□	□
Total	1.441	31	□	□	□

Table 4.9: Bead Height ANOVA Table;Removal of X2\*X5

Source	Sum Sq.	d.f.	Mean Sq.	F	Prob>F
X1	0.025	1	0.025	1.262	0.275
X2	0.066	1	0.066	3.256	0.086
X3	0.181	1	0.181	9.002	0.007
X4	0.232	1	0.232	11.496	0.003
X5	0.05	1	0.05	2.471	0.132
X1*X2	0.036	1	0.036	1.781	0.197
X2*X3	0.168	1	0.168	8.357	0.009
X2*X4	0.164	1	0.164	8.146	0.01
X3*X4	0.012	1	0.012	0.613	<b>0.443</b>
X3*X5	0.079	1	0.079	3.929	0.061
X4*X5	0.025	1	0.025	1.259	0.275
Error	0.403	20	0.02	□	□
Total	1.441	31	□	□	□



Table 4.10: Bead Height ANOVA Table; Removal of X3\*X4

Source	Sum Sq.	d.f.	Mean Sq.	F	Prob>F
X1	0.025	1	0.025	1.286	0.27
X2	0.066	1	0.066	3.318	0.083
X3	0.181	1	0.181	9.171	0.006
X4	0.232	1	0.232	11.711	0.003
X5	0.05	1	0.05	2.517	0.128
X1*X2	0.036	1	0.036	1.814	0.192
X2*X3	0.168	1	0.168	8.513	0.008
X2*X4	0.164	1	0.164	8.299	0.009
X3*X5	0.079	1	0.079	4.003	0.059
X4*X5	0.025	1	0.025	1.282	<b>0.27</b>
Error	0.415	21	0.02	□	□
Total	1.441	31	□	□	□

Table 4.11: Bead Height ANOVA Table; Removal of X3\*X4

Source	Sum Sq.	d.f.	Mean Sq.	F	Prob>F
X1	0.025	1	0.025	1.131	0.299
X2	0.066	1	0.066	2.919	0.102
X3	0.181	1	0.181	8.07	0.01
X4	0.232	1	0.232	10.305	0.004
X5	0.05	1	0.05	2.215	0.151
X1*X2	0.036	1	0.036	1.596	0.22
X2*X3	0.168	1	0.168	7.491	0.012
X2*X4	0.164	1	0.164	7.302	0.013
X4*X5	0.025	1	0.025	1.128	0.3
Error	0.494	22	0.022	□	□
Total	1.441	31	□	□	□

Table 4.12: Comparison of Reduced Models for Bead Height Experiment A

Iteration	Rsquare	Adjusted Rsquare	Model Pval
0	0.7350	0.5168	0.0099
1	0.7340	0.5419	0.0049
2	0.7305	0.5603	0.0024
3	0.7266	0.5763	0.0011
4	0.7200	0.5867	0.0006
<b>5</b>	<b>0.7101</b>	<b>0.5915</b>	<b>0.0003</b>
6	0.6552	0.5353	0.0006

Equation 4.9 is a result of the regression taken from the 5th ANOVA iteration and Equations 4.10 - 4.18 are the reduced models for experiments A and B.

$$\begin{aligned}
 Height_A = & 0.0263 + 0.0048x_1 - 0.6191x_2 - 0.0479x_3 - 0.0190x_4 - 0.0004x_5 \\
 & + 0.0138x_2x_3 + 0.0007x_2x_4 + 0.0033x_3x_5 + 0.0001x_4x_5 \quad (4.9)
 \end{aligned}$$

$$\begin{aligned}
 Width_A = & 0.087x_1 - 0.1576x_2 + 9.9317x_3 - 1.3537x_4 - 0.06x_1x_3 \\
 & + 0.0065x_1x_4 + 0.0001x_1x_5 + 0.0292x_2x_3 + 0.0011x_2x_4 - 0.0006x_4x_5 \quad (4.10)
 \end{aligned}$$

$$\begin{aligned}
 Penetration_A = & -0.0075x_1 + 0.0683x_2 + 0.3612x_3 + 0.0003x_1x_5 \\
 & - 0.0095x_2x_3 - 0.0006x_2x_4 - 0.0086x_3x_4 - 0.0149x_3x_5 \quad (4.11)
 \end{aligned}$$

$$\begin{aligned}
HAZdepth_A = & -0.0068x_1 + 0.3959x_2 - 2.3603x_3 + 0.0008x_4 - 0.1328x_5 \\
& - 0.0014x_1x_2 + 0.0196x_1x_3 - 0.0001x_1x_4 + 0.0004x_1x_5 \\
& - 0.027x_2x_3 + 0.0005x_2x_4 - 0.0002x_2x_5 - 0.0046x_3x_4 \\
& + 0.0076x_3x_5 + 0.0009x_4x_5
\end{aligned} \tag{4.12}$$

$$\begin{aligned}
HAZwidth_A = & 0.0134x_1 + 1.3461x_2 - 10.2102x_3 - 0.0353x_4 - 0.3895x_5 \\
& - 0.0059x_1x_2 + 0.0697x_1x_3 - 0.0005x_1x_4 + 0.001x_1x_5 \\
& - 0.0609x_2x_3 + 0.0032x_2x_4 - 0.0001x_2x_5 - 0.0114x_3x_4 \\
& + 0.0264x_3x_5 + 0.0024x_4x_5
\end{aligned} \tag{4.13}$$

$$\begin{aligned}
Height_B = & 0.0466x_1 - 0.0389x_2 - 0.8802x_3 - 0.064x_4 - 0.0321x_5 \\
& - 0.0003x_1x_2 - 0.0019x_1x_3 + 0.015x_2x_3 + 0.0007x_2x_4 \\
& + 0.0001x_2x_5 - 0.0038x_3x_4 + 0.0033x_3x_5 + 0.0001x_4x_5
\end{aligned} \tag{4.14}$$

$$\begin{aligned}
Width_B = & 0.1312x_1 + 0.2484x_2 - 9.3344x_3 + 0.3906x_4 - 0.2711x_5 \\
& - 0.0017x_1x_2 + 0.0252x_1x_3 - 0.0026x_1x_4 + 0.0007x_1x_5 \\
& + 0.0168x_2x_3 + 0.0026x_2x_4 - 0.0005x_2x_5 + 0.0223x_3x_5 \\
& - 0.0002x_4x_5
\end{aligned} \tag{4.15}$$

$$\begin{aligned}
Penetration_B = & -0.0429x_1 + 0.1269x_2 + 0.0513x_3 + 0.0226x_4 \\
& + 0.0056x_1x_3 + 0.0003x_1x_5 - 0.0155x_2x_3 - 0.0007x_2x_4 \\
& + 0.0082x_3x_4 - 0.0148x_3x_5 + 0.0001x_4x_5
\end{aligned} \tag{4.16}$$

$$\begin{aligned}
HAZdepth_B = & 0.0234x_1 + 0.2343x_2 - 3.0604x_3 - 0.1634x_4 - 0.1092x_5 \\
& - 0.0008x_1x_2 + 0.0115x_1x_3 + 0.0003x_1x_5 - 0.0051x_2x_3 \\
& + 0.0005x_2x_4 + 0.0144x_3x_4 + 0.005x_3x_5
\end{aligned} \tag{4.17}$$

$$\begin{aligned}
HAZwidth_B = & -0.05x_1 + 1.5653x_2 - 18.4752x_3 - 0.2401x_4 - 0.5088x_5 \\
& - 0.0049x_1x_2 + 0.0907x_1x_3 - 0.0003x_1x_4 + 0.001x_1x_5 \\
& - 0.0519x_2x_3 + 0.0033x_2x_4 - 0.0001x_2x_5 - 0.0092x_3x_4 \\
& + 0.0264x_3x_5 + 0.0024x_4x_5
\end{aligned}
\tag{4.18}$$

## 4.6 Discussion of results

The experimental results relating weld process parameters and weld bead height, width, penetration, HAZ depth and HAZ width for experiment A are given in Table 4.13 and Table 4.14 for experiment B. From the ANOVA analysis it is observed that the measured responses are more sensitive for the operating range for experiment A. When considering experiment B, different results were revealed from the ANOVA analysis. As in experiment A, speed is a contributing factor for bead height but is not the most significant. The interaction of current and wire speed followed by the interaction of current and y-orientation are the most significant parameters affecting bead height. The operating range for experiment B shows that the response characteristics are not as sensitive to changes in factor levels. This is most likely due to the overpowering effect of current on the entire process. For lower current values the other factors are more significant with their effects on a response, but higher current values mask other effects that other factors might have contributed when current was not as large. The variation in HAZ width and height decreases as parameter values increased in the second experiment. The difference between high and low levels for

current in the first experiment was 20 amps. This difference was also used for the second experiment, which contributes to increased variation in bead height, width and penetration. This suggests that variation in bead height, width and penetration for the second experiment decreased by tightening the gap between high and low levels of current. Figure 4.4 (a) and (b) shows the measured and predicted data for Experiment A and Experiment B respectively, that were plotted against each other to show how well the models fit to the data, with the exception of some outliers. These models can be used for automated applications that require accuracies of under 0.5mm since the mean error in the predicted values for bead width and height is found to be less than 10 percent.

Table 4.13: Experiment A Model Error

Run	Height			Width			Pen Depth			HAZ Depth			HAZ Width		
	Measured (mm)	Predicted (mm)	Error (%)	Measured (mm)	Predicted (mm)	Error (%)	Measured (mm)	Predicted (mm)	Error (%)	Measured (mm)	Predicted (mm)	Error (%)	Measured (mm)	Predicted (mm)	Error (%)
1	1.46	1.44	1.31	8.25	7.35	10.8	1.42	1.4	1.08	5.45	5.15	5.58	15.32	14.73	3.87
2	1.08	1.21	11.69	8.32	7.55	9.21	1.43	1.66	15.73	4.32	4.14	4.06	11.55	12.13	5.06
3	0.93	1.07	15.51	4.96	6.4	29.12	1.12	1.51	34.64	4.61	4.48	2.83	11.16	12.69	13.73
4	1.14	0.95	16.83	6.47	5.89	8.91	2.2	1.76	19.89	4.56	4.55	0.15	13.55	12.94	4.52
5	1.41	1.36	3.86	6.63	7.23	9.08	1.98	1.95	1.45	4.8	4.95	3.23	12.96	13.94	7.55
6	1.26	1.32	4.75	6.87	7.43	8.09	1.34	1.3	2.66	4.61	4.41	4.37	13.58	12.93	4.78
7	1.17	0.99	15.48	6.7	6.27	6.43	2.11	2.23	5.74	4.73	4.2	11.27	13.45	11.67	13.2
8	1.03	1.07	3.48	5.62	5.76	2.5	1.72	1.58	7.88	4.06	4.73	16.39	12.87	13.51	4.94
9	1.2	1.34	11.43	7.3	6.97	4.48	1.87	1.76	6.03	5.64	5.71	1.27	16.41	15.81	3.64
10	1.13	1.1	2.43	7.2	7.17	0.31	2.4	2.01	16.2	4.75	4.51	5.1	13.56	13.07	3.61
11	1.42	1.25	11.84	5.59	6.45	15.54	1.38	1.61	16.65	4.72	5.26	11.35	14.45	15.07	4.29
12	1.02	1.13	10.77	6.06	5.94	1.83	1.85	1.86	0.55	5.68	5.13	9.74	15.46	15.17	1.89
13	1.62	1.53	5.73	6.89	7.43	7.89	2.15	2.11	1.67	5.37	4.98	7.23	14.38	13.81	3.99
14	1.67	1.49	10.69	7.48	7.63	2.04	1.12	1.47	31.01	3.47	4.23	21.99	11.25	12.65	12.45
15	1.32	1.44	9.24	7.98	6.91	13.43	2.31	2.14	7.39	3.92	4.43	13.11	12.41	12.83	3.42
16	1.36	1.52	11.3	6.59	6.4	2.82	1.26	1.49	18.48	5.09	4.76	6.48	15.08	14.52	3.73
17	1.78	1.58	11.1	6.54	6.85	4.78	1.38	1.05	23.66	4.81	4.98	3.56	14.74	14.33	2.77
18	1.23	1.35	9.67	6.48	7.15	10.29	1.54	1.71	10.9	4.24	4.46	5.13	13.32	12.99	2.44
19	1.14	1.22	6.74	9.92	8.5	14.26	1.28	1.16	9.34	4.28	4.29	0.17	12.28	12.09	1.55
20	1.19	1.09	8	6.99	8.09	15.8	1.39	1.81	30.4	4.87	4.84	0.65	13.53	13.59	0.45
21	1.45	1.5	3.32	5.94	5.52	7.01	1.44	1.6	11.11	4.48	5.18	15.68	14.08	14.94	6.08
22	1.56	1.46	6.25	5.93	5.82	1.89	1.46	1.36	7.04	5.78	5.11	11.52	15.61	15.19	2.72
23	1.09	1.13	3.81	6.37	7.17	12.6	2.04	1.88	7.85	4.49	4.4	2.07	12.86	12.47	3.07
24	1.03	1.21	17.32	7.81	6.76	13.4	1.7	1.64	3.69	5.23	5.4	3.31	14.82	15.55	4.95
25	1.29	1.31	1.79	5.6	6.47	15.55	1.15	1.41	22.26	5.36	4.97	7.33	12.45	13.07	4.95
26	1.09	1.08	1.06	6.91	6.77	2.02	1.8	2.06	14.46	3.74	4.24	13.4	10.34	11.58	12
27	1.23	1.23	0.17	9.33	8.56	8.29	1.38	1.26	8.8	4.48	4.48	0.08	13.09	12.12	7.43
28	1.14	1.11	2.99	8.43	8.14	3.34	2.26	1.91	15.36	4.58	4.83	5.51	13.63	13.47	1.17
29	1.35	1.5	11.35	6.28	5.73	8.83	1.87	1.76	5.73	4.66	4.63	0.65	12.73	12.45	2.17
30	1.46	1.47	0.51	6.51	6.02	7.52	1.77	1.52	14.12	4.57	4.36	4.63	13.89	12.55	9.61
31	1.45	1.42	2.21	7.31	7.81	6.93	1.71	1.79	4.58	4.35	4.05	6.8	10.52	11.28	7.18
32	1.65	1.49	9.4	6.37	7.4	16.23	1.47	1.55	5.15	5.02	4.86	3.23	14.02	14.21	1.39

Table 4.14: Experiment B Model Error

Run	Height			Width			Pen Depth			HAZ Depth			HAZ Width		
	Measured (mm)	Predicted (mm)	Error (%)	Measured (mm)	Predicted (mm)	Error (%)	Measured (mm)	Predicted (mm)	Error (%)	Measured (mm)	Predicted (mm)	Error (%)	Measured (mm)	Predicted (mm)	Error (%)
1	1.46	1.45	0.35	9.51	8.76	7.86	1.42	1.41	0.37	5.19	5.39	3.76	15.32	15.03	1.9
2	1.08	1.19	9.81	8.71	7.72	11.36	1.43	1.59	11.27	5.27	4.76	9.7	11.55	12.44	7.67
3	0.93	1.12	20.63	9.07	8.52	6.07	1.12	1.46	30.45	4.74	4.82	1.79	11.16	12.91	15.64
4	1.14	0.97	15.66	6.61	7.24	9.51	2.2	1.77	19.43	3.58	4.2	17.28	13.55	13.15	2.94
5	1.41	1.41	0.18	7.32	7.02	4.14	1.98	1.98	0.21	5.05	4.95	2	12.96	13.91	7.34
6	1.26	1.34	6.55	6.24	7.32	17.23	1.34	1.26	5.68	4.27	4.62	8.26	13.58	12.9	4.98
7	1.17	1	14.21	6.67	6.77	1.57	2.11	2.19	3.74	4.77	4.68	1.94	13.45	11.6	13.74
8	1.03	1.05	1.57	7.34	6.83	6.9	1.72	1.61	6.51	4.53	4.35	3.95	12.87	13.43	4.39
9	1.2	1.27	6.02	7.55	8.32	10.24	1.87	1.84	1.78	5.27	5.56	5.58	16.41	15.81	3.65
10	1.13	1.07	5.12	6.87	6.71	2.31	2.4	2.01	15.97	4.74	4.94	4.17	13.56	13.07	3.62
11	1.42	1.23	13.52	9.16	9.12	0.47	1.38	1.63	17.84	5.11	5.2	1.69	14.45	15.02	3.95
12	1.02	1.14	11.8	7.67	7.27	5.27	1.85	1.93	4.52	5.11	4.57	10.56	15.46	15.12	2.22
13	1.62	1.53	5.54	6.89	6.91	0.33	2.15	2.09	2.86	5.4	5.03	6.92	14.38	13.66	5.03
14	1.67	1.53	8.44	6.74	6.64	1.46	1.12	1.38	22.91	4.66	4.7	0.85	11.25	12.5	11.12
15	1.32	1.41	6.84	7.07	7.71	9.02	2.31	2.04	11.65	5.01	4.95	1.25	12.41	12.68	2.18
16	1.36	1.52	11.5	6.85	7.2	5.05	1.26	1.46	15.9	4.57	4.62	1.12	15.08	14.36	4.75
17	1.78	1.59	10.97	10.01	9.59	4.17	1.38	1.03	25.65	5.49	5.49	0.02	14.74	14.18	3.82
18	1.23	1.32	7.07	9.08	9.34	2.9	1.54	1.62	4.92	5.27	5.18	1.71	13.32	12.84	3.6
19	1.14	1.25	9.9	7.42	8.32	12.11	1.28	1.08	15.95	5.09	4.93	3.18	12.28	11.94	2.79
20	1.19	1.1	7.87	7.56	7.83	3.57	1.39	1.8	29.12	4.57	4.62	1.08	13.53	13.44	0.67
21	1.45	1.5	3.79	7.34	8.35	13.79	1.44	1.7	18.03	4.98	5.28	6.09	14.08	14.87	5.63
22	1.56	1.43	8.03	9.52	9.44	0.81	1.46	1.4	4.03	5.37	5.27	1.78	15.61	15.12	3.13
23	1.09	1.1	0.55	7.12	7.08	0.59	2.04	1.91	6.24	5.19	5.01	3.44	12.86	12.45	3.21
24	1.03	1.14	10.53	8.64	7.93	8.22	1.7	1.75	2.67	5.17	5	3.24	14.82	15.54	4.83
25	1.29	1.29	0.06	7.95	8.48	6.67	1.15	1.45	25.91	5.53	5.35	3.21	12.45	12.98	4.28
26	1.09	1.09	0.06	7.05	7.66	8.68	1.8	2.04	13.21	4.89	5.04	3.15	10.34	11.5	11.19
27	1.23	1.25	1.35	8.74	8.24	5.68	1.38	1.24	10.33	5.29	4.99	5.76	13.09	12.07	7.76
28	1.14	1.16	1.67	7.46	7.18	3.69	2.26	1.96	13.35	4.54	4.68	3.01	13.63	13.43	1.49
29	1.35	1.51	11.86	8.46	7.58	10.45	1.87	1.81	3.08	5.13	5.05	1.65	12.73	12.64	0.71
30	1.46	1.51	3.35	8.74	8.1	7.36	1.77	1.51	14.47	5.13	5.04	1.82	13.89	12.74	8.27
31	1.45	1.39	4.13	7.84	7.34	6.4	1.71	1.77	3.22	4.39	4.97	13.14	10.52	11.55	9.76
32	1.65	1.5	9	6.96	7.62	9.48	1.47	1.6	8.68	4.88	4.96	1.6	14.02	14.49	3.33



Tables 4.15 and 4.16 summarize the results of the fitted models after the iterative model reduction processes has been preformed.

Table 4.15: Experiment A Reduced Model Results

Response	$R^2$	Adj $R^2$	p	No. of model itterations
height	0.71	0.59	0.0003	5
width	0.57	0.39	0.0121	6
penetration	0.63	0.52	0.0006	8
HAZ depth	0.53	0.15	0.0422	1
HAZ width	0.71	0.47	0.0182	1

Table 4.16: Experiment B Reduced Model Results

Response	$R^2$	Adj $R^2$	p	No. of model itterations
height	0.73	0.56	0.0024	3
width	0.67	0.43	0.0224	2
penetration	0.64	0.48	0.0047	5
HAZ depth	0.59	0.36	0.0323	4
HAZ width	0.7	0.44	0.0249	1

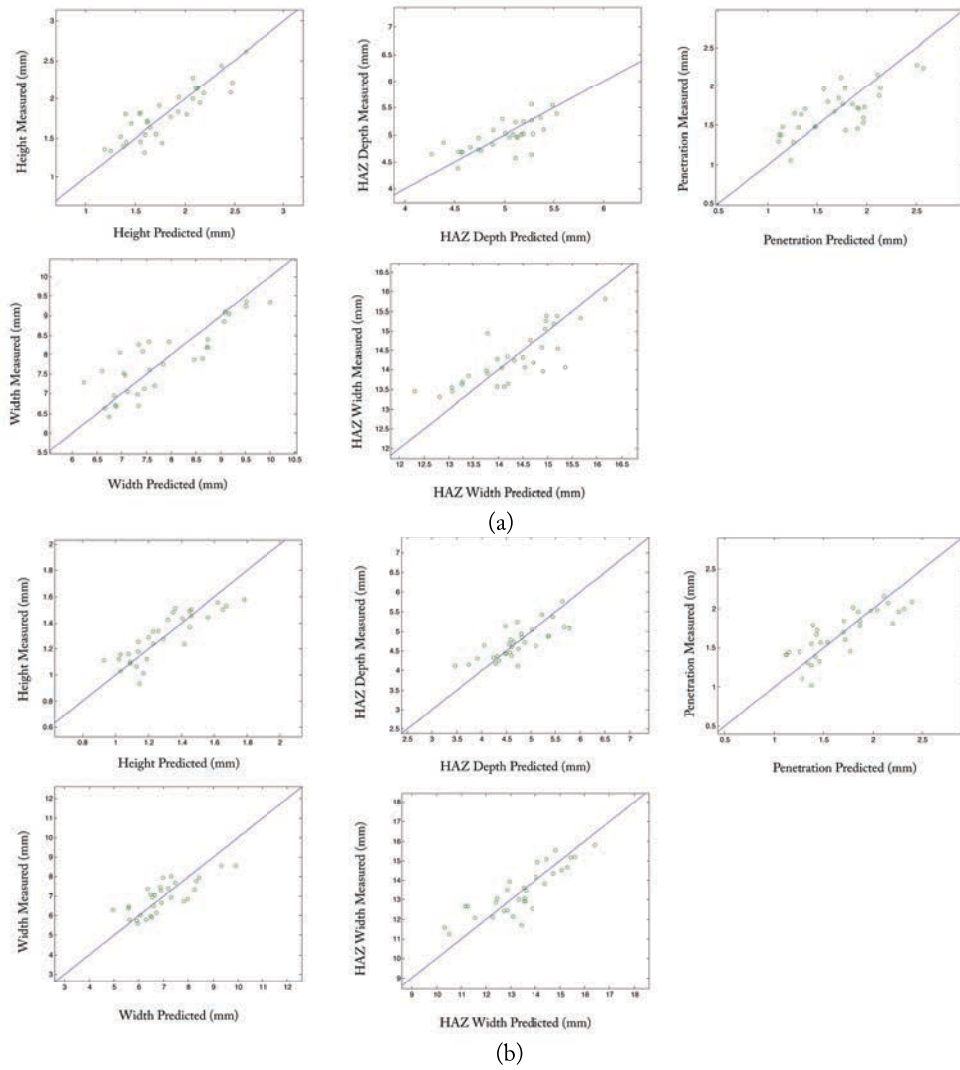


Figure 4.4: Measured vs. Predicted Response for Experiment B

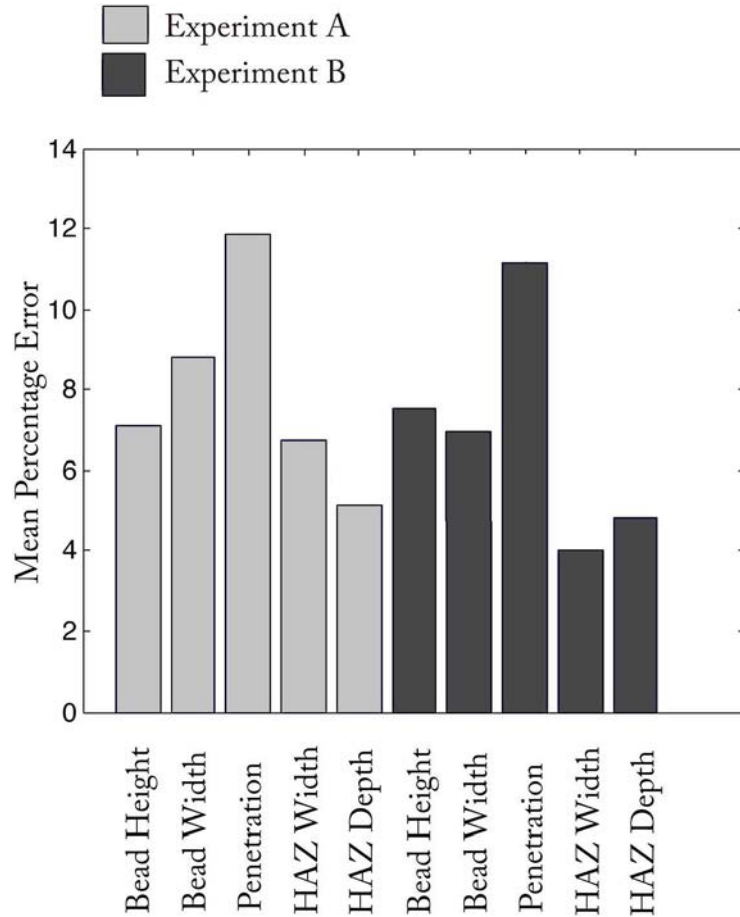


Figure 4.5: Average Percentage Error for experiments A and B

The mean of the percentage error for each response was evaluated and is shown in Figure 4.5. The main difference between the two experiments is that current, the main driving factor, was increased as well as the other factors that make up the response variables. A comparison between the mean error between these two experiments suggests that the variation in bead height, width and penetration increases as the controllable parameters are increased.

The two parameters x-orientation and y-orientation have been found to strongly influence the responses of bead height, width, penetration, heat affected zone width and

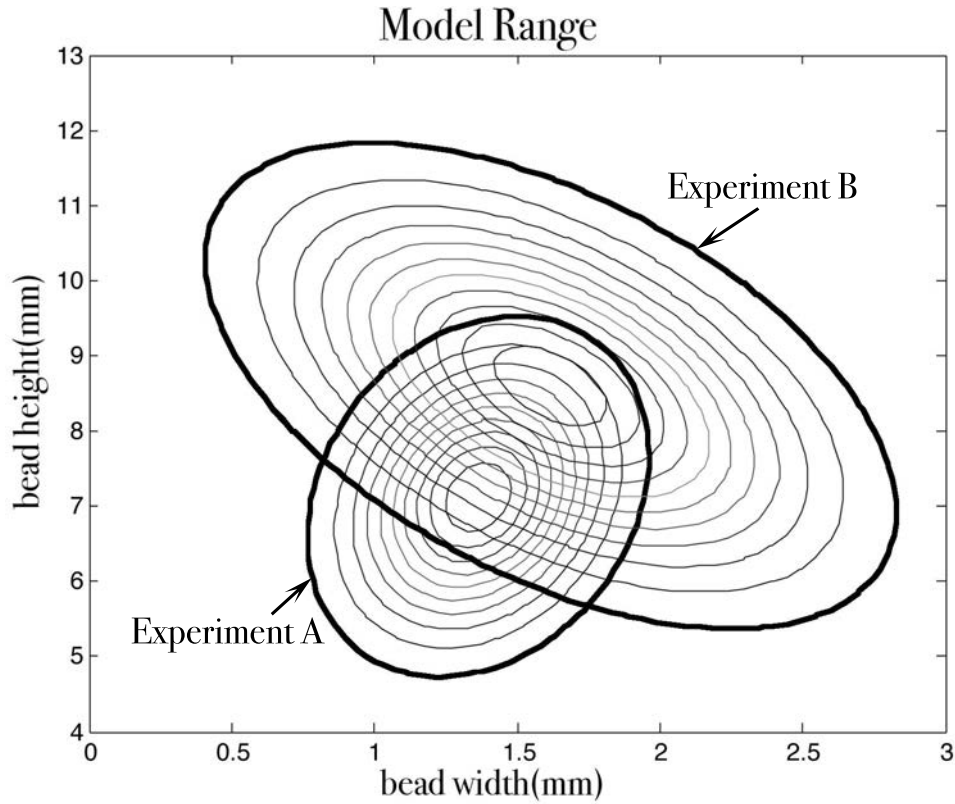


Figure 4.6: Boundary ranges containing 95% for models from experiment A and B

height. The interactions of these two parameters with current and wire feed rate significantly influence each response under the results of the ANOVA tables. These results suggest that base metal orientation is an important factor to be considered when predicting or controlling bead geometry of automated welding processes.

The output ranges of the models for bead width and height are shown in Figure 4.6. As described earlier, the influence of current on bead geometry is obvious as seen in the change in range distribution from experiment A to experiment B. The distribution of bead geometries for experiment A tend to have a positive slope. This occurs since variations in wire feed rate and robot speed will affect bead width and height proportionately. Thus producing tall and wide beads, short and skinny beads and beads of equal width and

height. The distribution of bead geometries for experiment B has a negative slope. This implies that the effect of current is more significant when compared to the proportional changes observed in experiment A. The result is more extreme geometries such as tall and skinny beads, as well as very wide and short beads. Multiple base metal orientations are included in the ranges and are within 0.5 millimeters of each other. Therefore multiple weld geometry exist that can be used for all base metal orientations within the ranges of the experiment. Intersecting ranges from both experiments can be used to produce same weld, which also contributes to the multiple weld geometries that are possible for any base metal orientation.

# Chapter 5

## Conclusions and Future Work

### 5.1 Conclusions

The goal of this study was to determine effects of welding parameters, namely gravitational, on GTAW geometry through experimentation and empirical model building. Automated GTA welding for refurbishing and repairing plastic injection molds was in need of a method for predicting bead geometry by adjusting controllable welding parameters. To provide this solution, the design and implementation of GTA welding experiments were performed to determine the effects of controllable parameters on weld height, width, penetration, heat affected zone width and heat affected zone depth. Using the fractional factorial design approach, the total number of runs in the experiments was reduced, allowing for multiple experiments and parameter ranges to be executed in a short period of time. A pilot experiment was performed to provide a general understanding of the welding process and the experimental welding process. Determining the relationships between GTA welding parameters carried out using conventional linear regression based on full factorial design

of experiments and the following conclusions have been reached:

- **Effects of base metal orientation** on bead geometry and penetration have been found to be significant. Interactions between current, wire feed and robot speed with base metal orientations was found to significantly contribute to variation in bead and penetration geometry.
- **Increasing parameter values** from experiment A to experiment B has resulted in more variation for bead width, height and penetration. This is mainly due to the sensitivity of bead geometry when an increase in parameter values for current, wire feed and robot speed, and their interactions with base metal orientations are present. Variation in heat affected zone width and height is found to decrease as parameter values were increased for experiment B. This is caused by increasing the heat input (current) for experiment B but using the same spacing between primary and background amperage. This difference between primary and background is less influential as current reaches high values.
- **Modeling results** depend strongly on experimental design and input parameter ranges. On average, the percentage error for width and height models was less than 10 percent, ie. 0.12mm error for a typical bead height of 1.2mm. Modeling errors for penetration were found to be to poorest at 11.5 and 14 percent for experiments A and B respectively.

## 5.2 Future Work

The following extensions are recommended for future work:

- A real-time controller should be considered in order to maintain a target weld bead geometry.
- A reliable automated welding system should have feedback, such as machine vision, to be used as an online tool for control for weld bead height and width.
- Wide and short beads will complete one layer quicker, but require more layers to be deposited. The opposite is known for using skinny tall beads. Therefore a optimal bead geometry should be selected to produce minimal stresses on the base metal.
- Artificial neural networks can be considered to improve generalization of predicted values for online use. Model reference adaptive control (MRAC) can be considered as a design scheme for online use.
- The goals of this topic can also be extend to other types of welding such as MIG or Laser welding and is not limited to multi-layer welding for refurbishment and repair plastic injection molds only.



# Appendix A

## Experimental Data

Table A.1: Measurements of L27 Experiment











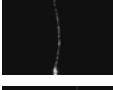

Run	Width(mm)	Height(mm)	Image
1	6.23	1.99	
2	6.52	1.44	
3	6.71	1.34	
4	5.56	1.08	
5	5.24	1.16	
6	5.19	1.75	
7	7.62	1.28	
8	4.94	1.28	
9	3.82	1.32	
10	5.99	1.82	
11	7.88	1.72	
12	5.13	1.94	

Table A.2: Measurements of L27 Experiment (cont')



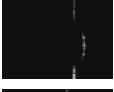




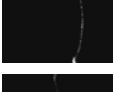







Run	Width(mm)	Height(mm)	Image
13	6.98	1.1	
14	4.95	1.45	
15	4.86	1.64	
16	4.45	1.3	
17	4.71	1.05	
18	5.35	1.36	
19	5.63	0.88	
20	7.66	0.93	
21	7.55	1.51	
22	4.32	1.44	
23	4.31	1.37	
24	3.96	1.35	
25	4.25	1.28	
26	4.8	1.41	
27	3.61	1.4	

Table A.3: GTAW DOE for experiments A and B

Run Number	A	B	C	D	E
1	-	-	-	-	-
2	-	-	-	-	+
3	-	-	-	+	-
4	-	-	-	+	+
5	-	-	+	-	-
6	-	-	+	-	+
7	-	-	+	+	-
8	-	-	+	+	+
9	-	+	-	-	-
10	-	+	-	-	+
11	-	+	-	+	-
12	-	+	-	+	+
13	-	+	+	-	-
14	-	+	+	-	+
15	-	+	+	+	-
16	-	+	+	+	+
17	+	-	-	-	-
18	+	-	-	-	+
19	+	-	-	+	-
20	+	-	-	+	+
21	+	-	+	-	-
22	+	-	+	-	+
23	+	-	+	+	-
24	+	-	+	+	+
25	+	+	-	-	-
26	+	+	-	-	+
27	+	+	-	+	-
28	+	+	-	+	+
29	+	+	+	-	-
30	+	+	+	-	+
31	+	+	+	+	-
32	+	+	+	+	+

Table A.4: Experiment A Results

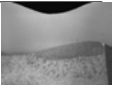











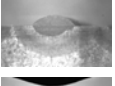

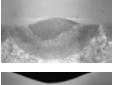

Run	Bead Height (mm)	Bead Width (mm)	Pen Depth (mm)	HAZ Depth (mm)	HAZ Width (mm)	Image
1	1.46	8.24	1.42	5.45	15.32	
2	1.08	8.32	1.43	4.32	11.55	
3	0.93	4.95	1.12	4.61	11.16	
4	1.14	6.46	2.19	4.56	13.55	
5	1.41	6.62	1.98	4.8	12.96	
6	1.26	6.87	1.34	4.61	13.58	
7	1.17	6.7	2.11	4.73	13.45	
8	1.03	5.62	1.72	4.06	12.87	
9	1.2	7.3	1.87	5.64	16.41	
10	1.13	7.19	2.39	4.75	13.56	
11	1.42	5.58	1.38	4.72	14.45	
12	1.02	6.05	1.85	5.68	15.46	
13	1.62	6.88	2.15	5.37	14.38	
14	1.67	7.48	1.12	3.47	11.25	
15	1.32	7.98	2.31	3.92	12.41	
16	1.36	6.58	1.26	5.09	15.08	

Table A.5: Experiment A Results (con't)






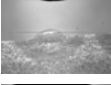
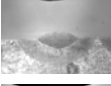
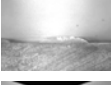


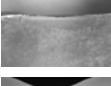
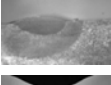
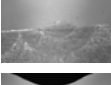
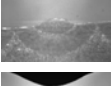
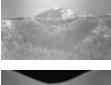

Run	Bead Height (mm)	Bead Width (mm)	Pen Depth (mm)	HAZ Depth (mm)	HAZ Width (mm)	Image
17	1.78	6.54	1.38	4.81	14.74	
18	1.23	6.48	1.54	4.24	13.32	
19	1.14	9.91	1.28	4.28	12.28	
20	1.19	6.98	1.39	4.87	13.53	
21	1.45	5.94	1.44	4.48	14.08	
22	1.56	5.93	1.46	5.78	15.61	
23	1.09	6.37	2.04	4.49	12.86	
24	1.03	7.8	1.7	5.23	14.82	
25	1.29	5.6	1.15	5.36	12.45	
26	1.09	6.9	1.8	3.74	10.34	
27	1.23	9.33	1.38	4.48	13.09	
28	1.14	8.42	2.26	4.58	13.63	
29	1.35	6.28	1.87	4.66	12.73	
30	1.46	6.51	1.77	4.57	13.89	
31	1.45	7.3	1.71	4.35	10.52	
32	1.65	6.36	1.47	5.02	14.02	

Table A.6: Experiment B Results


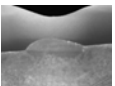

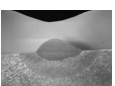
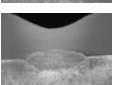

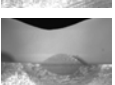
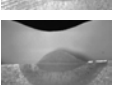
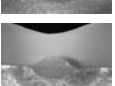
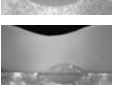
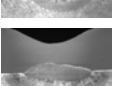
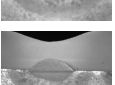
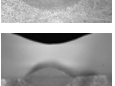
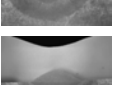

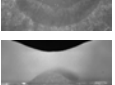
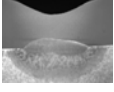
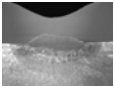
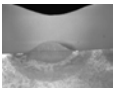
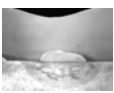
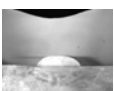

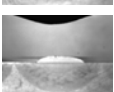
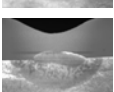
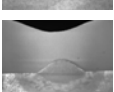
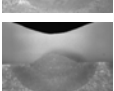
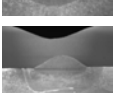
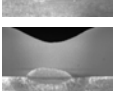

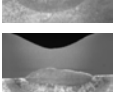
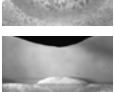

Run	Bead Height (mm)	Bead Width (mm)	Pen Depth (mm)	HAZ Depth (mm)	HAZ Width (mm)	Image
1	1.19	9.51	1.26	5.19	15.2	
2	1.6	8.71	1.79	5.27	15.36	
3	1.38	9.07	1.11	4.74	14.65	
4	2.02	6.61	1.23	3.58	13.06	
5	1.62	7.32	1.68	5.05	14.2	
6	2.11	6.24	1.38	4.27	12.31	
7	1.86	6.67	1.98	4.77	13.27	
8	2.37	7.34	1.13	4.53	13.98	
9	2.19	7.55	1.78	5.27	14.98	
10	1.94	6.87	1.74	4.74	13.76	
11	1.46	9.16	1.72	5.11	14.97	
12	1.93	7.67	1.97	5.11	14.91	
13	2.46	6.89	2.57	5.4	14.12	
14	2.08	6.74	2.51	4.66	12.82	
15	1.62	7.07	2.11	5.01	14.07	
16	2.13	6.85	1.61	4.57	13.79	

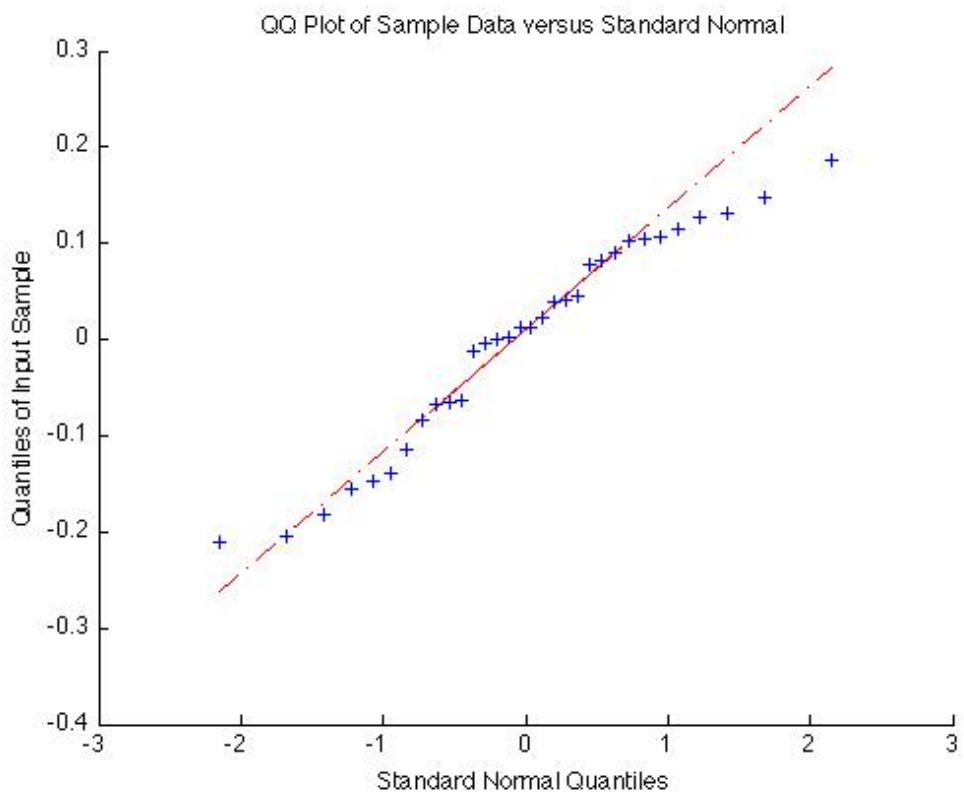
Table A.7: Experiment B Results (con't)

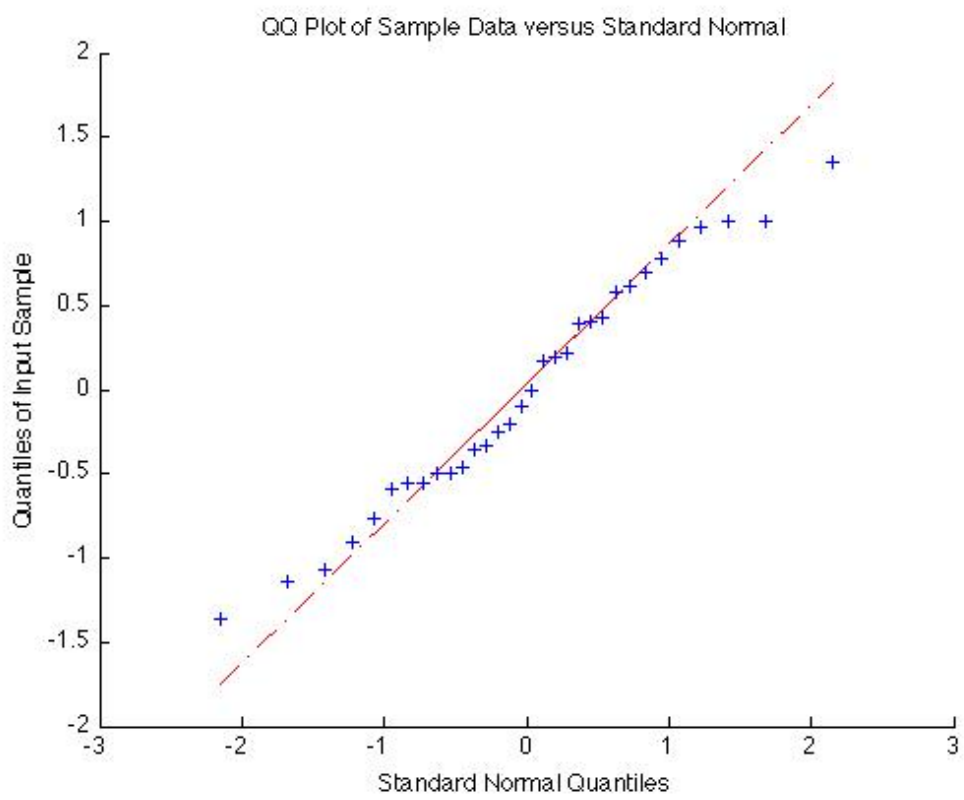
Run	Bead Height (mm)	Bead Width (mm)	Pen Depth (mm)	HAZ Depth (mm)	HAZ Width(mm)	Image
17	1.74	10.01	1.48	5.49	16.17	
18	1.71	9.08	1.31	5.27	14.96	
19	2.15	7.42	1.86	5.09	14.5	
20	1.54	7.56	1.11	4.57	13.28	
21	1.77	7.34	1.34	4.98	13.79	
22	1.25	9.52	1.97	5.37	15.67	
23	1.35	7.12	2.14	5.19	14.53	
24	1.65	8.64	1.49	5.17	14.89	
25	2.62	7.95	1.91	5.53	15.13	
26	2.08	7.05	1.92	4.89	14.19	
27	2.48	8.74	2.13	5.29	14.72	
28	1.55	7.46	1.15	4.54	13.07	
29	1.4	8.46	1.76	5.13	14.33	
30	1.55	8.74	1.27	5.13	15.21	
31	1.41	7.84	1.57	4.39	13.41	
32	1.59	6.96	1.9	4.88	13.98	

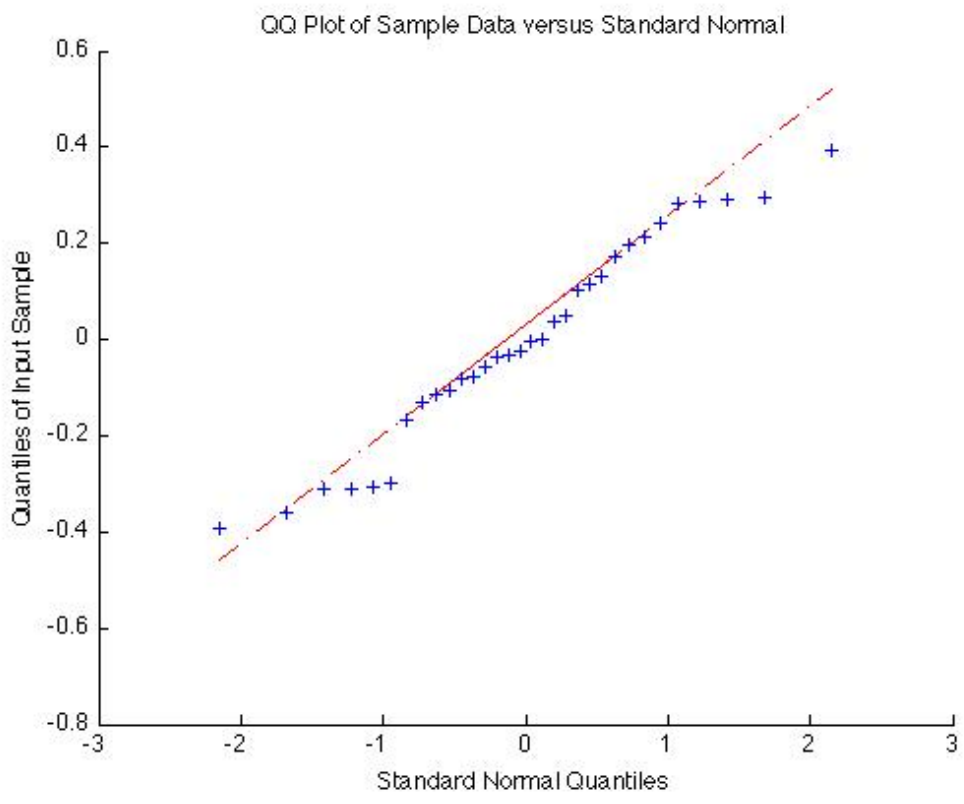


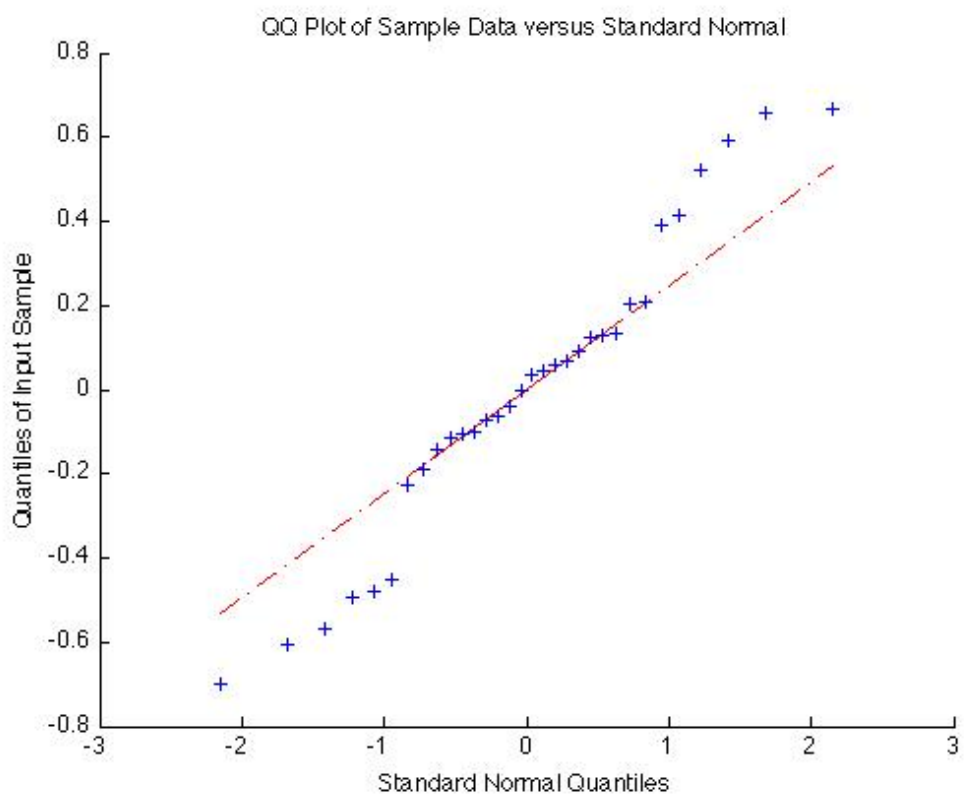
## Appendix B

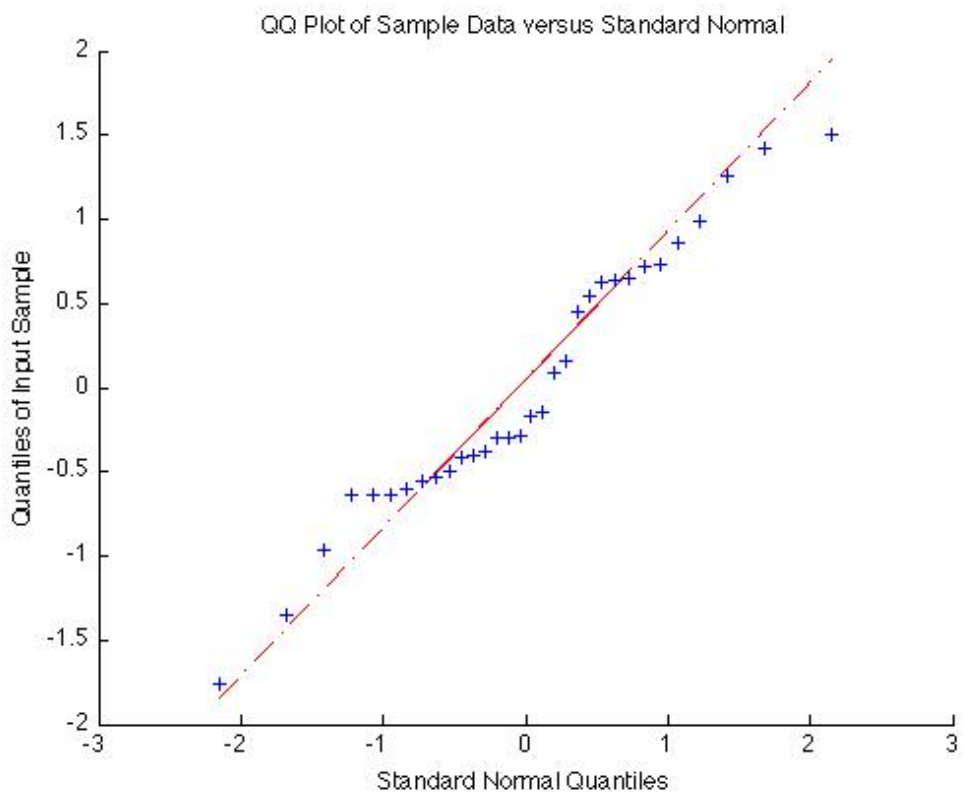
### QQ plots of residuals for Experiment A and B

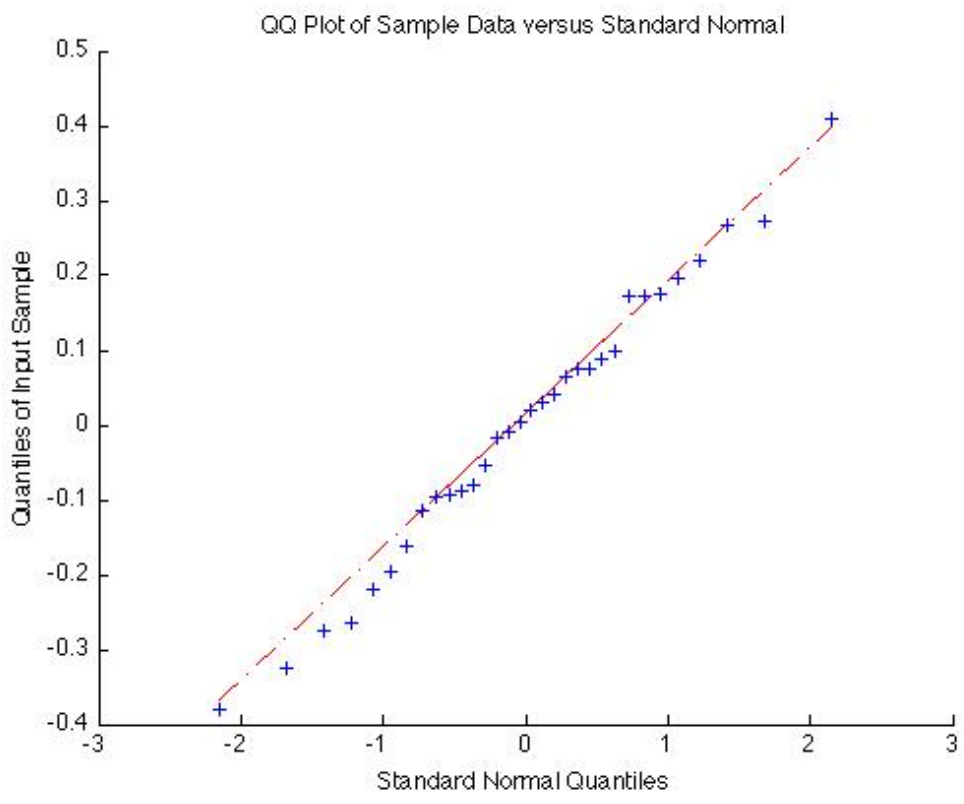


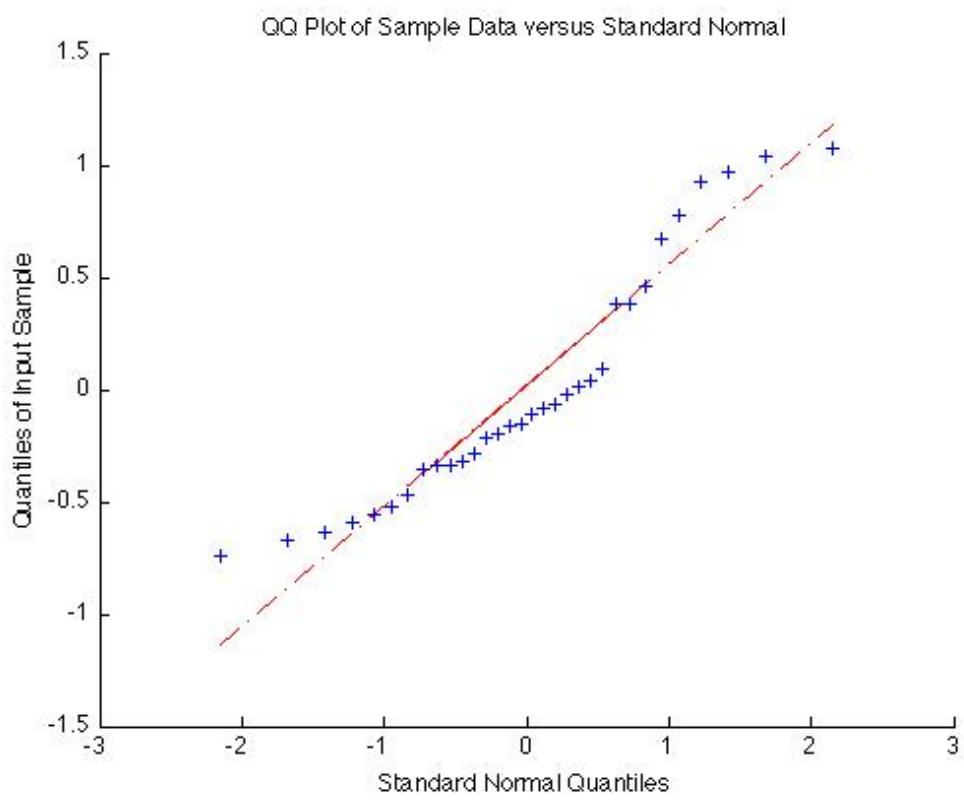




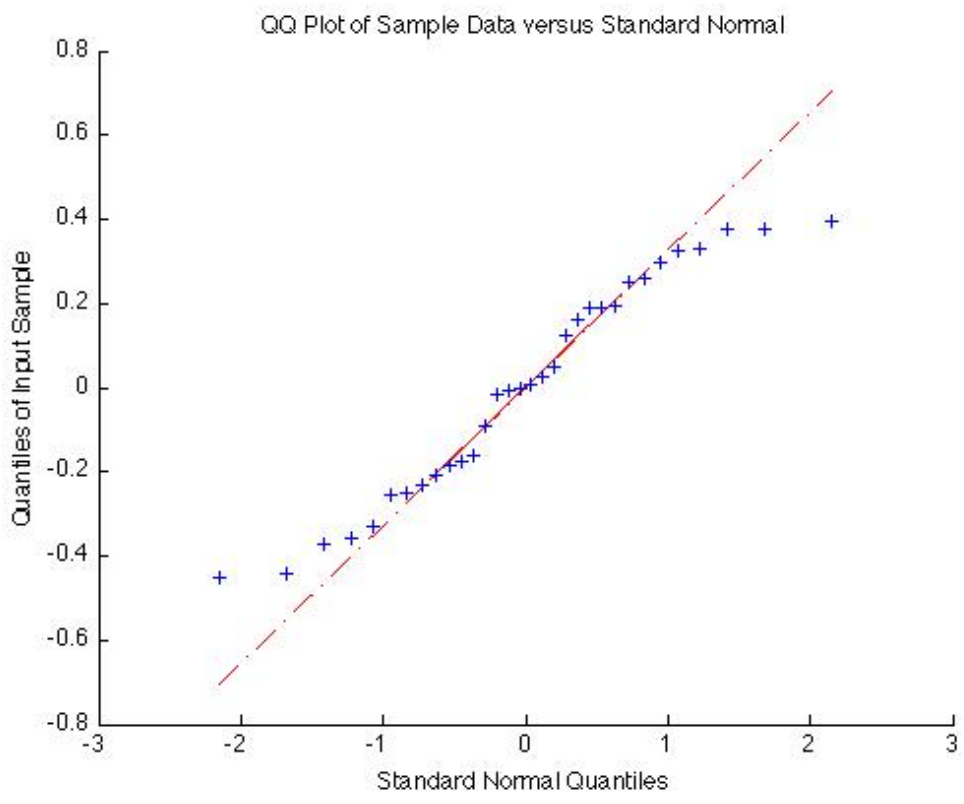


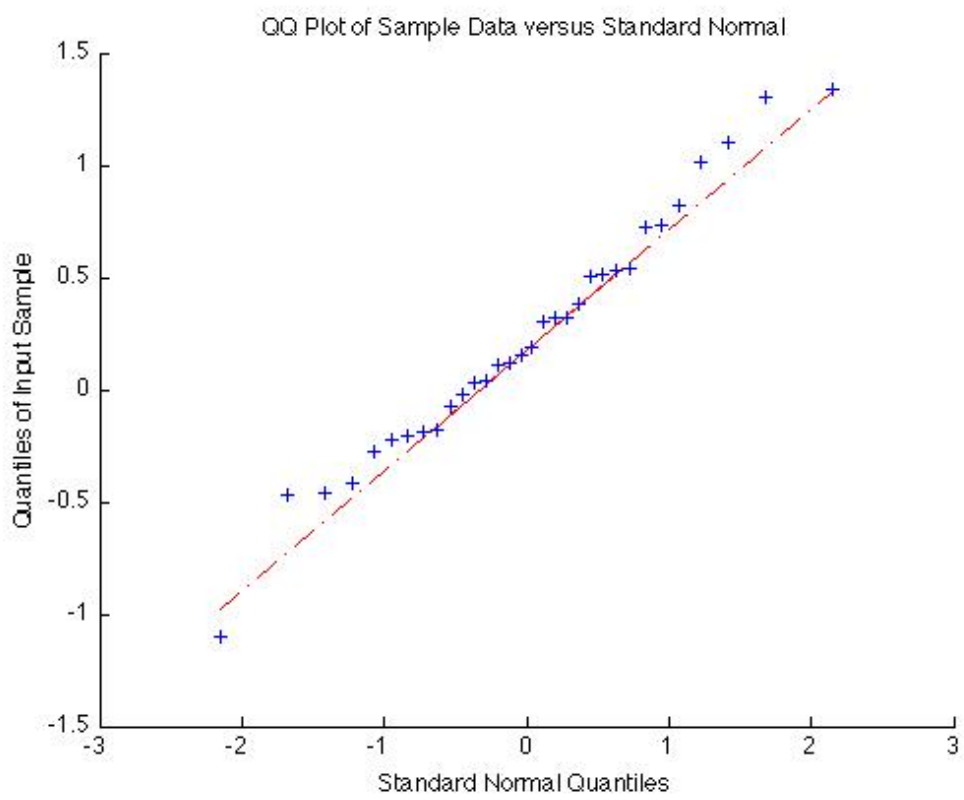


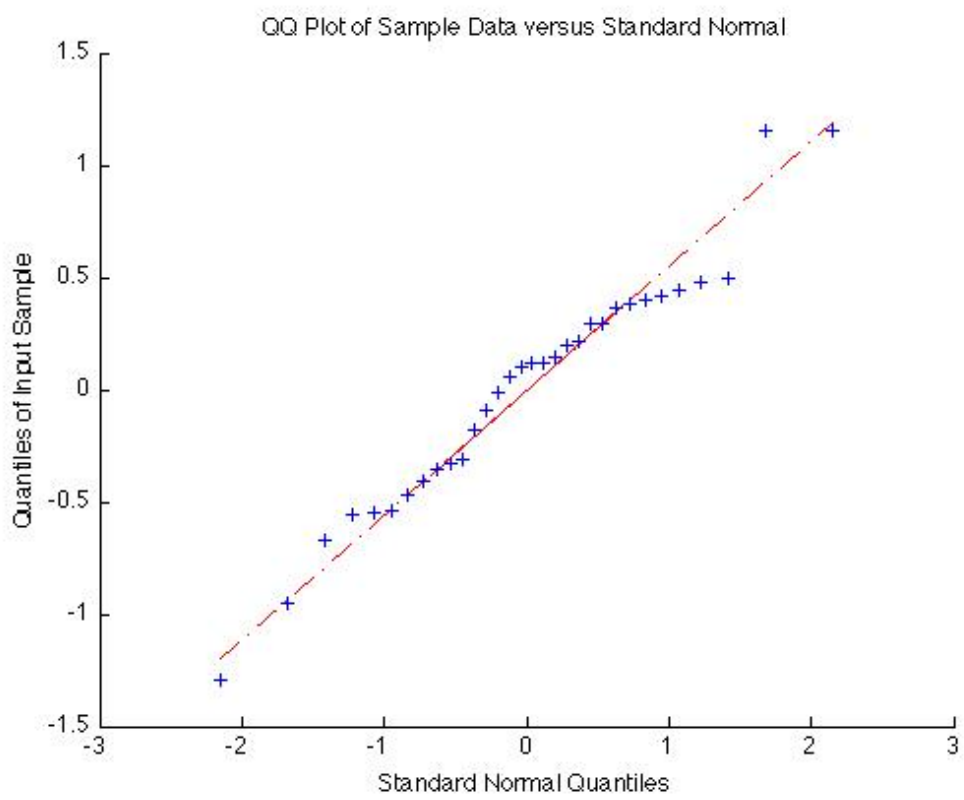












# Appendix C

## ANOVA Tables

Table C.1: Analysis of Variance - Bead Height Exp.A

Source	Sum Sq.	d.f.	Mean Sq.	F	Prob>F
Current	0.2295	1	0.2295	2.60989	0.12574
Wire	0.04575	1	0.04575	0.5203	0.48112
Speed	0.9765	1	0.9765	11.10471	0.00422
X Orientation	0.05865	1	0.05865	0.667	0.42609
Y Orientation	0.22278	1	0.22278	2.53341	0.13102
Current* Wire	0.1365	1	0.1365	1.5523	0.23073
Current*Speed	0.04728	1	0.04728	0.53764	0.47402
Current*X Orient	0.18758	1	0.18758	2.13312	0.16351
Current*Y Orient	0.07508	1	0.07508	0.85378	0.36921
Wire*Speed	0.003	1	0.003	0.03415	0.85571
Wire*X Orient	0.0657	1	0.0657	0.74717	0.40015
Wire*Y Orient	0.28313	1	0.28313	3.21971	0.09167
Speed*X Orient	0.06938	1	0.06938	0.78896	0.38757
Speed*Y Orient	0.06213	1	0.06213	0.70652	0.41299
X Orient*Y Orient	0.16388	1	0.16388	1.86361	0.1911
Error	1.40698	16	0.08794		
Total	4.03382	31			

Table C.2: Analysis of Variance - Bead Height Exp.B

Source	Sum Sq.	d.f.	Mean Sq.	F	Prob>F
Current	0.18758	1	0.18758	2.37319	0.14298
Wire	0.02258	1	0.02258	0.28565	0.60037
Speed	0.4209	1	0.4209	5.32515	0.03472
X Orientation	0.00015	1	0.00015	0.00194	0.96544
Y Orientation	0.003	1	0.003	0.03799	0.84791
Current* Wire	1.36538	1	1.36538	17.27438	0.00074
Current*Speed	0.00263	1	0.00263	0.03325	0.8576
Current*X Orient	0.003	1	0.003	0.03799	0.84791
Current*Y Orient	0.4632	1	0.4632	5.86032	0.02774
Wire*Speed	0.1164	1	0.1164	1.4727	0.24253
Wire*X Orient	0.01853	1	0.01853	0.23441	0.63483
Wire*Y Orient	0.10013	1	0.10013	1.26679	0.27697
Speed*X Orient	0.27195	1	0.27195	3.44068	0.08213
Speed*Y Orient	0.16388	1	0.16388	2.07334	0.16917
X Orient*Y Orient	0.081	1	0.081	1.02483	0.32644
Error	1.26465	16	0.07904		
Total	4.48497	31			

Table C.3: Analysis of Variance - Bead Width Exp.A

Source	Sum Sq.	d.f.	Mean Sq.	F	Prob>F
Current	6.31013	1	6.31013	10.58616	0.00498
Wire	7.00315	1	7.00315	11.74881	0.00345
Speed	4.3734	1	4.3734	7.33702	0.01549
X Orientation	0.0294	1	0.0294	0.04933	0.82705
Y Orientation	2.46975	1	2.46975	4.14337	0.05871
Current* Wire	1.7625	1	1.7625	2.95686	0.1048
Current*Speed	0.079	1	0.079	0.13254	0.72058
Current*X Orient	1.44925	1	1.44925	2.43133	0.13849
Current*Y Orient	0.02153	1	0.02153	0.03612	0.85167
Wire*Speed	0.79695	1	0.79695	1.337	0.26454
Wire*X Orient	1.35713	1	1.35713	2.27678	0.15082
Wire*Y Orient	0.9214	1	0.9214	1.54579	0.23167
Speed*X Orient	0.23978	1	0.23978	0.40226	0.53489
Speed*Y Orient	2.12695	1	2.12695	3.56827	0.07716
X Orient*Y Orient	2.06553	1	2.06553	3.46522	0.08115
Error	9.53717	16	0.59607		
Total	40.54305	31			

Table C.4: Analysis of Variance - Bead Width Exp.B

Source	Sum Sq.	d.f.	Mean Sq.	F	Prob>F
Current	2.12695	1	2.12695	3.8967	0.0659
Wire	0.91463	1	0.91463	1.67565	0.21387
Speed	0.50753	1	0.50753	0.92982	0.34926
X Orientation	0.68153	1	0.68153	1.2486	0.28032
Y Orientation	1.19738	1	1.19738	2.19367	0.158
Current* Wire	0.37195	1	0.37195	0.68144	0.42123
Current*Speed	0.86133	1	0.86133	1.578	0.22708
Current*X Orient	1.23638	1	1.23638	2.26512	0.1518
Current*Y Orient	1.66988	1	1.66988	3.05931	0.09943
Wire*Speed	0.84825	1	0.84825	1.55405	0.23048
Wire*X Orient	0.84825	1	0.84825	1.55405	0.23048
Wire*Y Orient	1.75313	1	1.75313	3.21183	0.09204
Speed*X Orient	0.44888	1	0.44888	0.82237	0.37794
Speed*Y Orient	0.0034	1	0.0034	0.00623	0.93804
X Orient*Y Orient	0.05865	1	0.05865	0.10746	0.74731
Error	8.73335	16	0.54583		
Total	22.26147	31			

Table C.5: Analysis of Variance - Penetration Depth Exp.A

Source	Sum Sq.	d.f.	Mean Sq.	F	Prob>F
Current	0.03578	1	0.03578	0.15498	0.69902
Wire	0.00008	1	0.00008	0.00034	0.98555
Speed	0.23633	1	0.23633	1.02368	0.3267
X Orientation	0.09138	1	0.09138	0.39581	0.53814
Y Orientation	0.01488	1	0.01488	0.06445	0.80284
Current* Wire	0.00263	1	0.00263	0.01138	0.91636
Current*Speed	0.0294	1	0.0294	0.12736	0.72585
Current*X Orient	0.0195	1	0.0195	0.08448	0.77505
Current*Y Orient	0.17258	1	0.17258	0.74754	0.40003
Wire*Speed	0.02153	1	0.02153	0.09325	0.76402
Wire*X Orient	0.06213	1	0.06213	0.26911	0.61103
Wire*Y Orient	1.5532	1	1.5532	6.72787	0.01959
Speed*X Orient	0.00138	1	0.00138	0.00597	0.93937
Speed*Y Orient	0.00025	1	0.00025	0.0011	0.97399
X Orient*Y Orient	0.0399	1	0.0399	0.17284	0.68312
Error	3.69378	16	0.23086		
Total	5.97472	31			

Table C.6: Analysis of Variance - Penetration Depth Exp.B

Source	Sum Sq.	d.f.	Mean Sq.	F	Prob>F
Current	0.32603	1	0.32603	1.9078	0.18619
Wire	0.02153	1	0.02153	0.12597	0.72728
Speed	0.01488	1	0.01488	0.08706	0.77174
X Orientation	0.00113	1	0.00113	0.0066	0.93625
Y Orientation	0.9214	1	0.9214	5.39172	0.03375
Current* Wire	0.13133	1	0.13133	0.76849	0.39366
Current*Speed	0.0294	1	0.0294	0.17206	0.6838
Current*X Orient	0.61328	1	0.61328	3.58868	0.0764
Current*Y Orient	0.00053	1	0.00053	0.00309	0.95636
Wire*Speed	0.00008	1	0.00008	0.00046	0.98321
Wire*X Orient	0.02258	1	0.02258	0.13212	0.721
Wire*Y Orient	0.10465	1	0.10465	0.61239	0.44532
Speed*X Orient	0.47288	1	0.47288	2.76711	0.11568
Speed*Y Orient	0.1815	1	0.1815	1.06209	0.31807
X Orient*Y Orient	0.05363	1	0.05363	0.31381	0.58311
Error	2.73428	16	0.17089		
Total	5.6291	31			

Table C.7: Analysis of Variance - HAZ Depth Exp.A

Source	Sum Sq.	d.f.	Mean Sq.	F	Prob>F
Current	0.02205	1	0.02205	0.064	0.8035
Wire	0.02645	1	0.02645	0.07677	0.78527
Speed	0.08	1	0.08	0.2322	0.63642
X Orientation	0.07605	1	0.07605	0.22074	0.64482
Y Orientation	0.13261	1	0.13261	0.38491	0.54372
Current* Wire	0.00245	1	0.00245	0.00711	0.93384
Current*Speed	0.0018	1	0.0018	0.00522	0.94327
Current*X Orient	1.0368	1	1.0368	3.00934	0.102
Current*Y Orient	0.15401	1	0.15401	0.44703	0.51328
Wire*Speed	0.5408	1	0.5408	1.56969	0.22825
Wire*X Orient	0.6272	1	0.6272	1.82047	0.19604
Wire*Y Orient	0.87781	1	0.87781	2.54787	0.13
Speed*X Orient	0.0648	1	0.0648	0.18808	0.67031
Speed*Y Orient	0.15961	1	0.15961	0.46328	0.50583
X Orient*Y Orient	0.04651	1	0.04651	0.135	0.71811
Error	5.51244	16	0.34453		
Total	9.3614	31			

Table C.8: Analysis of Variance - HAZ Depth Exp.B

Source	Sum Sq.	d.f.	Mean Sq.	F	Prob>F
Current	0.125	1	0.125	0.75706	0.39712
Wire	0.34031	1	0.34031	2.06109	0.17036
Speed	0.04651	1	0.04651	0.2817	0.60288
X Orientation	0.00011	1	0.00011	0.00068	0.9795
Y Orientation	0.00005	1	0.00005	0.0003	0.98633
Current* Wire	0.00045	1	0.00045	0.00273	0.95901
Current*Speed	0.06125	1	0.06125	0.37096	0.55103
Current*X Orient	0.04805	1	0.04805	0.29101	0.597
Current*Y Orient	0.18301	1	0.18301	1.10841	0.30807
Wire*Speed	0.83851	1	0.83851	5.07843	0.03861
Wire*X Orient	0.02531	1	0.02531	0.1533	0.70056
Wire*Y Orient	0.68445	1	0.68445	4.14536	0.05865
Speed*X Orient	0.09461	1	0.09461	0.57302	0.46006
Speed*Y Orient	0.00605	1	0.00605	0.03664	0.8506
X Orient*Y Orient	0.1458	1	0.1458	0.88303	0.36134
Error	2.6418	16	0.16511		
Total	5.24129	31			



Table C.9: Analysis of Variance - HAZ Depth Exp.A

Source	Sum Sq.	d.f.	Mean Sq.	F	Prob>F
Current	0.02205	1	0.02205	0.064	0.8035
Wire	0.02645	1	0.02645	0.07677	0.78527
Speed	0.08	1	0.08	0.2322	0.63642
X Orientation	0.07605	1	0.07605	0.22074	0.64482
Y Orientation	0.13261	1	0.13261	0.38491	0.54372
Current* Wire	0.00245	1	0.00245	0.00711	0.93384
Current*Speed	0.0018	1	0.0018	0.00522	0.94327
Current*X Orient	1.0368	1	1.0368	3.00934	0.102
Current*Y Orient	0.15401	1	0.15401	0.44703	0.51328
Wire*Speed	0.5408	1	0.5408	1.56969	0.22825
Wire*X Orient	0.6272	1	0.6272	1.82047	0.19604
Wire*Y Orient	0.87781	1	0.87781	2.54787	0.13
Speed*X Orient	0.0648	1	0.0648	0.18808	0.67031
Speed*Y Orient	0.15961	1	0.15961	0.46328	0.50583
X Orient*Y Orient	0.04651	1	0.04651	0.135	0.71811
Error	5.51244	16	0.34453		
Total	9.3614	31			

Table C.10: Analysis of Variance - HAZ Depth Exp.B

Source	Sum Sq.	d.f.	Mean Sq.	F	Prob>F
Current	0.125	1	0.125	0.75706	0.39712
Wire	0.34031	1	0.34031	2.06109	0.17036
Speed	0.04651	1	0.04651	0.2817	0.60288
X Orientation	0.00011	1	0.00011	0.00068	0.9795
Y Orientation	0.00005	1	0.00005	0.0003	0.98633
Current* Wire	0.00045	1	0.00045	0.00273	0.95901
Current*Speed	0.06125	1	0.06125	0.37096	0.55103
Current*X Orient	0.04805	1	0.04805	0.29101	0.597
Current*Y Orient	0.18301	1	0.18301	1.10841	0.30807
Wire*Speed	0.83851	1	0.83851	5.07843	0.03861
Wire*X Orient	0.02531	1	0.02531	0.1533	0.70056
Wire*Y Orient	0.68445	1	0.68445	4.14536	0.05865
Speed*X Orient	0.09461	1	0.09461	0.57302	0.46006
Speed*Y Orient	0.00605	1	0.00605	0.03664	0.8506
X Orient*Y Orient	0.1458	1	0.1458	0.88303	0.36134
Error	2.6418	16	0.16511		
Total	5.24129	31			

Table C.11: Analysis of Variance - HAZ Width Exp.A

Source	Sum Sq.	d.f.	Mean Sq.	F	Prob>F
Current	0.95565	1	0.95565	0.41666	0.52776
Wire	0.74115	1	0.74115	0.32314	0.57762
Speed	0.00878	1	0.00878	0.00383	0.95144
X Orientation	0.55388	1	0.55388	0.24149	0.62981
Y Orientation	3.8157	1	3.8157	1.66362	0.21545
Current* Wire	0.63563	1	0.63563	0.27713	0.60581
Current*Speed	0.03445	1	0.03445	0.01502	0.90398
Current*X Orient	12.86513	1	12.86513	5.6091	0.0308
Current*Y Orient	0.72903	1	0.72903	0.31785	0.58072
Wire*Speed	1.42383	1	1.42383	0.62078	0.44227
Wire*X Orient	2.91008	1	2.91008	1.26877	0.27661
Wire*Y Orient	0.01758	1	0.01758	0.00766	0.93133
Speed*X Orient	4.96913	1	4.96913	2.1665	0.16044
Speed*Y Orient	0.26828	1	0.26828	0.11697	0.7368
X Orient*Y Orient	0.3507	1	0.3507	0.1529	0.70093
Error	36.69785	16	2.29362		
Total	66.97685	31			

Table C.12: Analysis of Variance - HAZ Width Exp.B

Source	Sum Sq.	d.f.	Mean Sq.	F	Prob>F
Current	0.69915	1	0.69915	0.9877	0.3351
Wire	1.6974	1	1.6974	2.39795	0.14105
Speed	0.10238	1	0.10238	0.14463	0.70872
X Orientation	0.0075	1	0.0075	0.0106	0.91928
Y Orientation	0.28313	1	0.28313	0.39998	0.53603
Current* Wire	1.06945	1	1.06945	1.51083	0.23678
Current*Speed	0.322	1	0.322	0.4549	0.50965
Current*X Orient	0.15263	1	0.15263	0.21562	0.64865
Current*Y Orient	0.8224	1	0.8224	1.16182	0.29707
Wire*Speed	3.10628	1	3.10628	4.38829	0.05246
Wire*X Orient	0.50753	1	0.50753	0.71699	0.40962
Wire*Y Orient	1.43228	1	1.43228	2.0234	0.17409
Speed*X Orient	0.3507	1	0.3507	0.49544	0.49163
Speed*Y Orient	0.2329	1	0.2329	0.32903	0.57421
X Orient*Y Orient	0.43478	1	0.43478	0.61422	0.44465
Error	11.3257	16	0.70786		
Total	22.54622	31			

# References

- [1] “Tig handbook, chapter 1 - the gtaw (tig) process.” xii, 5
- [2] *Welding handbook*. Miami, FL: Miami, FL : American Welding Society, - 2001. 13
- [3] D. Rosenthal, “The theory of moving sources of heat and its application to metal treatments,” *American Society of Mechanical Engineer Transactions*, vol. 68, pp. 849–866, 1946. 13
- [4] M. Goodarzi, R. Choo, and J. Toguri, “The effect of the cathode tip angle on the gtaw arc and weld pool: I. mathematical model of the arc,” *Journal of Physics D: Applied ...*, Jan 1997. [Online]. Available: <http://iopscience.iop.org/0022-3727/30/19/013>  
13
- [5] M. Goodarzi, R. Choo, and T. Takasu, “The effect of the cathode tip angle on the gas tungsten arc welding arc and weld pool: Ii. the mathematical model for the weld pool,” *Journal of Physics D: ...*, Jan 1998. [Online]. Available: <http://iopscience.iop.org/0022-3727/31/5/014>
- [6] Z. Cao, Z. Yang, and X. Chen, “Three-dimensional simulation of transient gma weld pool with free surface,” *WELDING JOURNAL-NEW YORK-*, Jan 2004. [Online]. Available: <http://12.176.97.197/wj/supplement/wj0604-169.pdf>

- [7] H. Y. S. Y. Fenggui Lu, Xinhua Tang, “Numerical simulation on interaction between,” *Journal of Materials Processing Technology*, vol. Volume 189, pp. Pages 352–366, Jan 2006.
- [8] M. U. J. L. M Tanaka, H Terasaki, “A unified numerical modeling of stationary tungsten-inert-gas welding process,” *Metallurgical and Materials Transactions A*, vol. Volume 33, pp. 2043–2052, Jun 2007. 13
- [9] J. Hu and H. Tsai, “Heat and mass transfer in gas metal arc welding. part ii: The metal,” *International Journal of Heat and Mass Transfer*, Jan 2007. [Online]. Available: <http://linkinghub.elsevier.com/retrieve/pii/S0017931006004923> 14
- [10] —, “Heat and mass transfer in gas metal arc welding. part i: The arc,” *International Journal of Heat and Mass Transfer*, Jan 2007. [Online]. Available: <http://linkinghub.elsevier.com/retrieve/pii/S001793100600490X> 14
- [11] A. R. C. J.P. Ganjigatti, Dilip Kumar Pratihari, “Global versus cluster-wise regression analyses for prediction of bead geometry in mig welding process,” *Journal of Materials Processing Technology*, pp. 1–15, Jul 2010. 14
- [12] U. Esme, A. Kokangul, M. Bayramoglu, and N. Geren, “Mathematical modeling for prediction and optimization of tig welding pool geometry,” *Metallurgija*, Jan 2009. 14
- [13] I. Kim, K. Son, Y. Yang, and P. Yaragada, “Sensitivity analysis for process parameters in gma welding processes using a factorial design method,” *International Journal of Machine ...*, Jan 2003. [Online]. Available: <http://linkinghub.elsevier.com/retrieve/pii/S0890695503000543> 15

- [14] Y. Song, S. Park, and S. Chae, “3d welding and milling: part ii—optimization of the 3d welding process using an experimental design approach,” *International Journal of Machine Tools and ...*, Jan 2005. [Online]. Available: <http://linkinghub.elsevier.com/retrieve/pii/S0890695504003086> 15
- [15] Y. Song, S. Park, D. Choi, and H. Jee, “3d welding and milling: Part ia direct approach for freeform fabrication of metallic prototypes,” *International Journal of Machine Tools ...*, Jan 2005. [Online]. Available: <http://linkinghub.elsevier.com/retrieve/pii/S0890695504003074> 15
- [16] W. Cao and Y. Miyamoto, “Freeform fabrication of aluminum parts by direct deposition of molten aluminum,” *Journal of Materials Processing Technology*, Jan 2006. [Online]. Available: <http://linkinghub.elsevier.com/retrieve/pii/S0924013605009532> 16
- [17] Y. Zhang, Y. Chen, P. Li, and A. Male, “Weld deposition-based rapid prototyping: a preliminary study,” *Journal of Materials Processing Tech.*, Jan 2003. 16
- [18] C. Atwood, M. Ensz, D. Greene, and M. Griffith, “Laser engineered net shaping (lens (tm)): A tool for direct fabrication of metal parts,” ... *on Applications of ...*, Jan 1998. [Online]. Available: [http://www.osti.gov/energycitations/product.biblio.jsp?osti\\_id=1549](http://www.osti.gov/energycitations/product.biblio.jsp?osti_id=1549) 16
- [19] K. Taminger and R. Hafley, “Electron beam freeform fabrication: a rapid metal deposition process,” *Proceedings of the 3rd Annual Automotive ...*, Jan 2003. [Online]. Available: <http://www.cs.odu.edu/~mln/ltrs-pdfs/NASA-2003-3aacc-kmt.pdf> 17
- [20] L. Zadeh, “Fuzzy sets,” *Information and Control* 8 (3), pp. 338–353, 1965.

- [21] W. Z. C.H. Kim and T. DebRoy, “Modeling of temperature field and solidified surface profile during gas metal arc fillet welding,” *Journal of Applied Physics*, vol. 94, no. 4, 2003.
- [22] A. E. T. Zacharia, “Three-dimensional transient model for arc welding process,” *Metallurgical and Materials Transactions B*, vol. 20, no. 5, pp. 645–659, 1989.
- [23] K. Hong, D. Weckman, A. Strong, and W. Zheng, “Modelling turbulent thermofluid flow in stationary gas tungsten arc weld pools,” *Science and Technology of Welding Joining*, vol. Volume 7, no. Number 3, pp. pp. 125–136(12), June 2002.
- [24] A. Mackwood and R. Crafer, “Thermal modelling of laser welding and related processes: a literature review,” *Optics & Laser Technology*, Jan 2005. [Online]. Available: <http://linkinghub.elsevier.com/retrieve/pii/S0030399204000507>
- [25] P. Murray and A. Scotti, “Depth of penetration in gas metal arc welding,” *Science and Technology of Welding*, Jan 1999. [Online]. Available: <http://www.ingentaconnect.com/content/maney/stwj/1999/00000004/00000002/art00007>
- [26] Y. T. S.C. Juang, “Process parameter selection for optimizing the weld pool geometry in the tungsten inert gas welding of stainless steel,” *Journal of Materials Processing Technology*, pp. pp. 54–62, Jul 2010.